UNIVERSITY OF OKLAHOMA

GRADUATE COLLEGE

THE EFFECTS OF EVAPORATION AND CAPILLARY FORCES ON FLUID MOTION, SOLUTE TRANSPORT, AND WATER CONTENT FROM THE GRAIN SCALE TO THE CONTINUUM SCALE IN UNSATURATED POROUS MEDIA

A DISSERTATION

SUBMITTED TO THE GRADUATE FACULTY

in partial fulfillment of the requirements for the

Degree of

DOCTOR OF PHILOSOPHY

By

ADERONKE OMOWUMI ADEGBULE

Norman, Oklahoma

2019

Downloaded from SHAREOK. Persistent Handle URL: https://hdl.handle.net/11244/321508

THE EFFECTS OF EVAPORATION AND CAPILLARY FORCES ON FLUID MOTION, SOLUTE TRANSPORT, AND WATER CONTENT FROM THE GRAIN SCALE TO THE CONTINUUM SCALE IN UNSATURATED POROUS MEDIA

A DISSERTATION APPROVED FOR THE
SCHOOL OF CIVIL ENGINEERING AND ENVIRONMENTAL SCIENCE

BY THE COMMITTEE CONSISTING OF

Dr. Tohren Kibbey, Chair

Dr. Randall Kolar

Dr. David Sabatini

Dr. Gerald Miller

Dr. Jeffrey Harwell

© Copyright by ADERONKE OMOWUMI ADEGBULE 2019

All Rights Reserved.

This material is based upon work supported by the National Science Foundation under Grant No. 1446264. The work in Chapter 2 was also partially supported by the National Science Foundation under Grants No. 1336083 and 1336579.

Chapter 2 has been previously published as “The Effect of Sand Grain Roughness on the Grain-Scale Spatial Distribution of Grain-Surface Precipitates Formed by Evaporation” in *Colloids and Surfaces A: Physicochemical and Engineering Aspects*, 2018 and is used here by permission.

ACKNOWLEDGEMENTS

I would first want to express my gratitude to God whose grace and providence has made the completion of my PhD program a reality.

I would like to thank my advisor, Dr. Kibbey for his all-round support throughout the program. His suggestions and expertise were invaluable in formulating my research topic and methodology. Most impactful on me was his positive attitude. He always saw good in every situation. His encouraging words kept me going through tough times when I felt like giving up. I am grateful for the privilege to learn from him.

I would also like to thank my committee members, Dr. Kolar, Dr. Sabatini, Dr. Miller and Dr. Harwell for their time and contribution to my research.

I would like to acknowledge Dr. Charalambos Papelis of the New Mexico State University and Shang Yan, my colleague at the University of Oklahoma for collaborating with me on some of my work.

I would also like to acknowledge Dr. Preston Larson for his help with SEM imaging, Dr. Andrew Madden for his contribution to my writing, Mike Schmidt and Dennis McAlister for their help with fabricating and assembling items for my experiments.

Last but not the least, I will like to appreciate my entire family for being there for me. My mother was that sympathetic ear I could always count on. She always believed I would succeed. To my brother Kunle, thank you for taking time out of your busy schedule to critique my writing and help me think through challenges. To my husband Gbenga, thank you for always believing in me and being a wall of support through this stressful period. To my children Faith, Jeremiah

and Joy, thank you for your unconditional love. You guys were always a happy distraction to ease my mind when I was stressed with work.

Table of Contents

Acknowledgements……..….iv

List of Figures…….viii

List of Tables……ix

Abstract……..x

Chapter 1. Introduction……..1
1.1 Background……..1
1.2 Motivation……..……..4
1.3 Research Objectives……5

Chapter 2. The Effect of Sand Grain Roughness on the Grain-Scale Spatial Distribution of Grain-Surface Precipitates Formed by Evaporation…….7
Abstract…….……7
2.1 Introduction……..……8
2.2 Materials and Methods……10
2.2.1 Materials……..…….10
2.2.2 Experimental procedures……..11
2.2.3 Numerical Simulation……..……12
2.3 Results and Discussion……14
2.4 Conclusions…….26

Chapter 3. The Relationship Between Microscopic Grain Surface Structure and the Dynamic Capillary-Driven Advance of Water Films over Individual Dry Natural Sand Grains….28
Abstract……..…28
3.1 Introduction……..28
3.1.1 Movement of capillary films over rough surfaces……31
3.1.2 Objectives…….32
3.2 Materials and Methods……..……..33
3.2.1 Materials……..…….33
3.2.2 Experimental procedures……..34
3.2.3 Image Processing……..35
3.3 Results and Discussion……36
3.4 Conclusions…….52

Chapter 4. Exploring te Impact of Long-Term Evaporation on the Relationship Between Capillary Pressure and Water Saturation in Unsaturated Porous Media……..53
Abstract……..…53
4.1 Introduction……...……..54
4.2 Materials and Methods……...….56
4.2.1 Materials……...56
4.2.2 Experimental procedure……...…56

4.3 Results and Discussion……59
4.4 Conclusions…….....70

Chapter 5. Summary and Conclusions…….….72
5.1 Conclusions…….....72
5.2 Recommendations for Future Work……74

References…….....75

List of Figures

Figure 2.1. SEM images of the two quartz sand grains used in the study, Grains A and B…...15

Figure 2.2. Calculated high resolution elevation maps for Grains A and B……16

Figure 2.3. Precipitation of sodium chloride (A, B) and sucrose (C, D) on Grain A. SEM images are shown at left, while images with EDS overlays are shown at right……....17

Figure 2.4. Precipitation of sodium chloride (A, B) and sucrose (C, D) on Grain B. SEM images are shown at left, while images with EDS overlays are shown at right……18

Figure 2.5. Model-simulated precipitation of sodium chloride (0.2 M) on Grain B……21

Figure 2.6. Schematic illustrating the source of currents in water films during evaporation…...22

Figure 2.7. Precipitation of sucrose (A) and sodium chloride (B) from high concentration solutions on glass microscope slides…….24

Figure 2.8. Model-simulated precipitation of sucrose (0.05 M) on Grain B, calculated based on the revised model that includes viscosity effects……..26

Figure 3.1. Schematic showing the contact angle and the surface energies acting on the contact line for a drop of liquid on a solid surface exposed to vapor phase……..30

Figure 3.2. Figure showing the process of liquid being wicked along a surface groove…….30

Figure 3.3. Schematic of the experimental setup showing reservoir containing dyed water connected by a hypodermic tubing to contact the grain……....35

Figure 3.4. Images of Grain 1: A. SEM image. B. Edge map. C. Filtered edge density map..…37

Figure 3.5. Images showing flow of dyed water across Grain 1……..38

Figure 3.6. Inlet positions on Grain 1, numbered from 1 to 9……..40

Figure 3.7. Plot of initial wicking velocity versus distance along path for points 1 through 9 showing minimum, maximum and average initial wicking velocities of the flow experiments at that point……41

Figure 3.8. Plot of edge density versus distance along path superimposed on a plot of initial wicking velocity versus distance along path for points 1 through 9. Plot shows minimum, maximum and average initial wicking velocities observed during flow experiments at that point and the measured edge density of the inlet position……..42

Figure 3.9. Images of Grain 2: A. SEM image. B. Edge map. C. Filtered edge density map...…43

Figure 3.10. Images showing flow of dyed water across Grain 2…….44

Figure 3.11. Images showing side by side comparisons of the edge density maps with the observed wicking pattern for Grains 1 and 2. The red dots indicate where the wicking started: A. Filtered edge density map for Grain 1. B. Observed wicking pattern on Grain 1. C. Filtered edge density map for Grain 2. D. Observed wicking pattern on Grain 2……..45

Figure 3.12. Images of Grain 3: A. SEM image. B. Edge map. C. Filtered edge density map….46

Figure 3.13. Images of Grain 4: A. SEM image. B. Edge map. C. Filtered edge density map….46

Figure 3.14. High magnification SEM images of Grain 1 showing surface roughness in form of micro-porosity. Surface contains holes of varying sizes as well as some undulations……..47

Figure 3.15. High magnification SEM images of Grain 2 showing surface roughness in form of undulation with some isolated holes……..48

Figure 3.16. Images showing water spreading over concrete surface in 3 second intervals…….49

Figure 3.17. Images showing plots of distance versus square root of time for: A. Grain 1 and B. Grain 2……...……51

Figure 4.1. Schematic of the experimental system used for F30 Sand. A. Front view of the optical cell. B. Top view of the optical cell. C. Side view of the entire imaging system……..57

Figure 4.2. Images of F30 sand showing imbibition, and then drainage/evaporation over 60 days. The closed system is on the left, and the open system is on the right. Brighter pixels correspond to higher saturation. Note that images have been shifted vertically to align water levels, which were allowed to drop gradually during drainage……...……61

Figure 4.3. P_c-S curves for the F30 sand showing spontaneous imbibition curves (in red), and drainage curves corresponding to evaporation over 117 days (in blue). Curves shown correspond to A. the closed system, and B. the open system. Times of selected curves are labeled…….62

Figure 4.4. Comparison between P_c-S curves in the open and closed systems for F30 sand, showing spontaneous imbibition, and drainage curves after 117.7 days of evaporation……..64

Figure 4.5. Elevation vs. time at four saturation levels in the F30 sand for the A. closed and B. open systems…….65

Figure 4.6. Ratio of elevation in open and closed systems vs. time at four saturation levels in the F30 sand……66

Figure 4.7. Images of the membrane showing imbibition, and then drainage/evaporation over 48h……67

Figure 4.8. Imbibition and drainage (evaporation) for the membrane. Note that subsequent experiments found that the true drainage curve is above the top of the membrane; evaporation causes saturation to decrease until the curve matches the imbibition P_c-S curve…….……68

Figure 4.9. Drainage/evaporation of a membrane followed by rapid imbibition induced by covering the reservoir to slow evaporation. The plot shows the elevation of the portion of the membrane where S=0.4 as a function of time. The arrow indicates the time the reservoir was covered……...……...69

List of Tables

Table 3.1. Table showing the initial wetting front/wicking velocities observed on experimental grains and concrete……50

Abstract

This work aimed to explore how fluid motion, solute transport, and water content are influenced by evaporation and capillary forces in unsaturated porous media, across a range of scales. Experiments were conducted from the grain scale to the continuum scale to explore a range of related flow phenomena.

The effect of solid surface roughness on precipitate formation has been widely studied for several years in different disciplines. However, few studies exist which studied precipitation on natural sand grains. In this study, the patterns of deposits formed on individual natural sand grain surfaces from solutions of sodium chloride and sucrose were studied. The patterns were studied using Scanning Electron Microscope (SEM) imaging and Energy Dispersive Spectroscopy (EDS). Results showed that as evaporation progressed, flow tended to occur towards the ridges, likely as a result of the discrepancy between the water configuration demanded by capillarity and the spatial distribution of evaporation. In the case of the sodium chloride solution, this led to sodium chloride precipitates being deposited on the ridges. For the sucrose solution, the outward flow was retarded by its viscosity at high concentrations. As a result, the sucrose was trapped in the valleys and precipitated there.

The impact of surface roughness on liquid wicking over a dry surface was also studied. While several studies exist on wicking on engineered surfaces, very few studies exist on wicking over natural surfaces. This study examined wicking patterns on dry individual sand grains. The roughness of the grains was studied using a combination of SEM imaging and edge detection to generate edge density maps. The wicking pattern was studied by taking regular images of the grain using an optical microscope. Sulforhodamine B dye was used in the water to make it easy to see the water on the sand grains. The results suggest that microporosity is required for rapid

wicking. On grains which exhibited wicking, the liquid was wicked onto the rougher portion of the grain as shown by the edge density map. However, between grains, edge density maps alone are not sufficient to predict flow.

Finally, the effect of evaporation on capillary pressure-saturation (P_c-S) curves of two porous media was studied. The media were saturated and then allowed to drain. A test sample was exposed to evaporation after drainage while the control sample was not. Both samples were backlit, and images were taken at regular interval as the experiment progressed. The images were analyzed using a computer program which related light transmission to saturation. Results showed that evaporation lowered the drainage curve of both samples towards the imbibition curves. The rate of the lowering depended on the rate of evaporation experienced by the sample relative to the volume of the sample.

Chapter 1

Introduction

1.1 Background

In unsaturated soils, moisture exists mainly as water films covering the surface of the soil grains. The hydraulic behavior of water films is very different from bulk water, which is predominant in the saturated zone of a soil. To understand the processes which occur in the unsaturated zone, it is important to study how water films behave and how their behavior affects processes occurring in soil.

The unsaturated zone of a soil is the portion of soil above the water table. The water table is the upper level of the zone of saturation. Below the water table, the soil is completely saturated, with soil pores completely filled up with water. Above the water table, soil pores are partly saturated with water and partly with air. The water table is at atmospheric pressure. Water above the water table is at negative pressure relative to the water table and the pressure gets progressively more negative as it nears the ground surface. Exposure to the atmosphere at the ground surface causes continuous evaporation of porewater. Thus, a significant amount of flow taking place in the unsaturated zone, especially in very low moisture soils, is in the gaseous phase (Tuller & Or, 2005), or driven by evaporation. As water saturation decreases, the air-water interfacial area increases (Kibbey & Chen, 2012). The processes of flow, solute transport, and mass transfer in the unsaturated zone differ significantly from what is obtained in the saturated zone because of the presence of air-water interfaces (Gray & Hassanizadeh, 1991).

Nonsteady-state flow in the unsaturated zone could be uniform or non-uniform. Non-uniform flow results in an unstable (irregular) wetting front which causes the flow to occur faster

at some locations on the wetting front compared with others. Non-uniform flow is also known as preferential flow and could be caused by a number of factors, including heterogeneity in the unsaturated zone (Hendrickx & Flury, 2001). Under natural conditions, the most significant flow in the unsaturated zone tends to occur vertically. Water drains downwards towards the saturated zone due to gravity. Water can also be lost from the top of the soil through evaporation from the soil surface and transpiration through the leaves of plants. Downward drainage will continue until a certain moisture content known as the residual moisture content, a moisture content where retained water is held by capillary forces, but has limited hydraulic continuity. At moisture contents below the residual moisture content, water will no longer drain out under gravity and can only be lost upwards through evaporation/transpiration (Rhoades et al., 2015).

Capillary pressure refers to the pressure difference across the interface between two fluids within the voids in a porous medium. Saturation refers to the volume of a specified fluid contained in the voids of a Representative Elementary Volume (REV) of a porous medium with respect to the total volume of voids in an REV of the porous medium (Bear, 1972). The capillary pressure-saturation (P_c-S) curve is an important relationship needed to understand multiphase flow in a porous medium. For any simulation involving multiphase flow in a porous medium, the (P_c-S) curves are an important input. Flow in the vadose zone is usually multiphase, involving air, water and in many cases, some other non-aqueous organic fluid such as an oil or organic liquid contaminant. The concept of hysteresis in (P_c-S) curves means that at a certain capillary pressure, a porous medium can exhibit varying saturation levels based on how the moisture content was reached. The saturation reached by draining a porous medium is higher than that reached by imbibition. Understanding the (P_c-S) relationship helps us determine the saturation

expected in a porous medium relative to the water table. It enables the identification of regions of saturation and regions dominated by air pockets and water films.

Water in unsaturated soils is mainly held by capillary forces and adsorption. Capillary-held water can exist in pores between grains, as well as on the surfaces of grains. As matric potentials increase, and moisture levels drop, capillary-held thin films on grain surfaces play an increasingly important role in liquid water movement in unsaturated media (Peters & Durner, 2008; Lebeau & Konrad, 2010).

Studies have led to the belief that at residual moisture contents, most of the moisture retained in a soil exists as adsorbed films (Tuller & Or, 2005). The films are thought to be nanometers (nm) thick with thicknesses decreasing as capillary pressure increases. The thinness of these films makes it difficult for flow to occur in them. As a result, their existence in a soil retards flow (Tokunaga, 2009, 2011), diffusion (Hu & Wang, 2003) and transport through the soil (Saiers & Lenhart, 2003; Shang et al., 2008). These adsorbed films can form when water vapor in low moisture soils contact hydrophilic soil grain surfaces. The Van der Waal forces of attraction between the two cause the vapor to condense into thin films on the grain surface (Butt & Kappl, 2009). Studies have shown that the moisture content of a soil is proportional to its specific surface area when the soil is dominated by adsorbed water films (Tuller & Or, 2005).

Capillary held water films are capable of sustaining high flow rates when they form interconnected networks (Peters & Durner, 2008; Tokunaga, 2009). These films form on depressions in sand grains and at grain-to-grain contact points. They are thicker by orders-of-magnitude than adsorbed films (Kibbey, 2013).

1.2 Motivation

At moisture contents above the residual moisture content, film thicknesses are controlled by the capillary pressure (Tokunaga & Wan, 1997; T. W. Kim *et al.*, 2013). Recent studies have found that at the residual moisture content of soil, most of the water films remain capillary-held (Kibbey, 2013; T. W. Kim *et al.*, 2013). These film thicknesses have been shown to remain relatively constant at moderate capillary pressures. This is because at residual moisture content, the water films are controlled by grain roughness. The receding water films are pinned on the peaks on the grain surfaces preventing further thinning (Kibbey, 2013). The implication of this is that even below residual moisture contents, many flow-dependent processes such as contaminant transport are still possible in natural porous media made up of individual grains with high roughness.

This study seeks to increase our understanding of the hydraulic behavior of capillary films, and to generate quantitative data on its impact on flow, transport and mass transfer. Mass transfer in the unsaturated zone takes place at fluid-fluid interfaces (e.g., the water-air interface in water films) (Kibbey & Chen, 2012). It is therefore important to understand how the configuration of water films vary with environmental processes such as evaporation and drainage. Advection and diffusion of dissolved solutes as well as mass transfer such as evaporation depend upon mixing in the media involved. Surface tension and temperature gradients in water films can generate mixing within the films, which will in turn promote transport of dissolved solutes or nanoparticles through dispersion, diffusion, or advection.

1.3 Research Objectives

The first objective of this work is to get an increased understanding of the effect of surface roughness on contaminant precipitation from water films. In several applications, including cleaning dielectric substrates, space craft cleaning, indoor ventilation/particle removal, and soil remediation, precipitation from solution, and the related problem of particle deposition and removal are important issues (Borodin *et al.*, 2009; Zhong *et al.*, 2010; Probst *et al.*, 2011; Wang *et al.*, 2012; Muthiah *et al.*, 2013). This is because in the course of time, with exposure to the environment, dissolved solutes can be precipitated from solution and deposited at interfaces as water content decreases. In partially saturated systems, a significant number of these interfaces occur on solid surfaces. Understanding the effect of roughness on precipitation will not only increase understanding of the likely locations of precipitation, but also shed light on how it will affect the subsequent removal of such deposits. Chapter 2 explores how grain surface structure influences the patterns of precipitation on individual grains resulting from evaporation.

The second objective is to understand the role that grain surface roughness plays in the patterns of liquid wicking over its surface. In several applications, such as convective boiling systems (B. S. Kim *et al.*, 2016) and oil and gas recovery, it is desirable to control the direction of flow. Surface structure has been shown to impact wicking (B. S. Kim *et al.*, 2014). The study includes grain scale studies of roughness on actual sand grains. Understanding the effect of roughness on wicking patterns at grain scale will ultimately enhance our understanding of its effects at the continuum scale. Chapter 3 describes a range of wicking experiments conducted on single grains to better understand how grain structure influences wicking.

The last objective is to study the effect of evaporation on Capillary pressure-saturation (P_c-S) curves. The P_c-S curve is a very important parameter in designs involving unsaturated porous

media. The capillary pressure-saturation curve for a given porous medium will vary depending on how the moisture content in the medium was reached, either by water draining out from the saturated medium or through water being drawn by capillary forces into a dry medium (Imbibition). The moisture content achieved through imbibition is usually lower that the moisture content achieved through drainage. The work studies the effect of prolonged evaporation on drained porous media, to understand how long-term evaporation influences the observed relationship between capillary pressure and saturation. Chapter 4 describes long-term evaporation experiments conducted to explore this question.

Chapter 2

The Effect of Sand Grain Roughness on the Grain-Scale Spatial Distribution of Grain-Surface Precipitates Formed by Evaporation

Abstract

This work examined the precipitation patterns formed by two solutes (sucrose, sodium chloride) on individual sand grains after evaporation from aqueous solution. Experiments were conducted by placing droplets of solution on individual grains, allowing them to evaporate, and then imaging the resulting precipitates. Grains were cleaned and used for multiple experiments with different solution concentrations. Precipitation patterns were studied through a combination of scanning electron microscope (SEM) imaging and energy dispersive x-ray spectroscopy (EDS). The results of the work found that sodium chloride precipitates were formed on ridges on the grain surfaces, while sucrose precipitates were formed in valleys. The difference in the behavior was consistent with the hydraulics of film flow out of low points on grain surfaces during evaporation, and the different viscosities of the two solutes near their solubilities. Simulations were able to produce precipitation patterns on grain surfaces consistent with experimental observations. Based on the results of the work, it is likely that most solutes will exhibit precipitation on ridges; only those with extremely high viscosities at their solubility (e.g. hundreds of cP) might be expected to be trapped in valleys.

---

* This chapter has been published as "The effect of sand grain roughness on the grain-scale spatial distribution of grain-surface precipitates formed by evaporation." by Adegbule, A. O., Yan, S., Papelis, C., & Kibbey, T. C. in *Colloids and Surfaces A: Physicochemical and Engineering Aspects*, 2018

2.1 Introduction

Evaporation of a solvent in natural or engineered porous media can cause the concentrations of nonvolatile dissolved solutes in porewater to increase progressively until the compounds precipitate out of solution onto grain surfaces and in the surrounding pores. In an environmental context, the spatial configurations of precipitates can potentially impact the dynamics of redissolution in porous media by impacting the accessible interfacial area across which dissolution can occur, potentially influencing the ultimate mobility of the compounds in the environment. In an industrial context, an understanding of factors impacting precipitation on rough surfaces could be useful in a range of situations, such as controlling unwanted surface deposition during processes involving evaporation. The focus of this work was on studying how grain-surface roughness impacts patterns of chemical precipitation on individual grain surfaces, with the ultimate goal of developing a more quantitative understanding of how precipitates form on rough surfaces.

Noninvasive imaging methods such as dual energy gamma radiation, x-ray micro tomography and magnetic resonance imaging (MRI) have been used to study processes occurring in porous media (Singurindy & Berkowitz, 2005; Werth *et al.*, 2010; Zhang *et al.*, 2011; Darbha *et al.*, 2012; Helliwell *et al.*, 2013). A significant amount of work has been reported studying the patterns of salt precipitation in sands as a result of evaporation. The effects of factors such as grain size, grain angularity, grain hydrophobicity, grain size distribution, ambient temperature and salt type on precipitation patterns have been studied (McKinley *et al.*, 2006; Kamai *et al.*, 2009; Nachshon *et al.*, 2011; Rad, 2014; Weisbrod *et al.*, 2014; Bergstad & Shokri, 2016). While surface precipitation is widely observed to occur, many of these studies have focused on patterns

of precipitation formed in pore spaces, in part because of their impact on permeability and evaporation patterns.

Across various disciplines, the related phenomena of surface precipitation and deposition on surfaces has been studied using imaging technology like scanning electron microscopy (SEM) and transmission electron microscopy (TEM) (Wang *et al.*, 2010; Reddy *et al.*, 2011; Tao & Salmeron, 2011; Kibsgaard *et al.*, 2012). For example, research has shown that rougher surfaces tended to retain a higher number of nanoparticles in the environment (Darbha *et al.*, 2012). In the medical sciences, the effect of surface morphology on precipitation patterns was studied and it was found that roughness was critical to bioactivity of metals to be used as implants. The ability of apatite to precipitate out from simulated body fluids onto treated metal strips was greatly enhanced by surface roughness (Chen *et al.*, 2008). Studies have shown that for ceramic materials to be used as bone implants, surface roughness of the ceramic material greatly improved the rate of apatite formation from simulated body fluids in vitro (Hou *et al.*, 2011). Surface roughness also increased precipitation of calcium phosphate on phospholipid layers (Yang *et al.*, 2014).

Despite the extensive studies done on evaporation/precipitation in saline rich soils, the mechanisms behind the process are not yet fully understood (Nachshon & Weisbrod, 2015). While numerous studies have been performed on representative elementary volumes (REVs) of sand, thus giving some understanding of precipitation in pores, relatively less work has been done to understand the evaporation/precipitation process at the grain scale (Meakin & Tartakovsky, 2009). In the same vein, much data exists on precipitation of NaCl and other inorganic salts on rough surfaces but relatively fewer studies have been done on precipitation of organic substances as a result of evaporation. Studies of precipitation patterns formed on rough

surfaces in saturated environments exist, but these surfaces are usually reactive with precipitation occurring as a result of some chemical reaction or adsorption of ions to the surface. Little work has been reported examining surface precipitation in unsaturated systems due only to evaporation.

The hypothesis driving this work was that the evaporation process would cause thicker precipitates to form in the deeper valleys on grain surfaces and thinner precipitates on the plateaus, as a result of solute concentration increasing as capillary held water films recede to low points on the grain. As the water evaporates, the air-water interface recedes gradually towards the grain surface, forming a liquid film which initially bridges the high points on the grain. As evaporation progresses, regions of thick film on solid surfaces shrink to occupy hydraulically disconnected regions with lower-elevation surface roughness features (Kibbey, 2013). It was hypothesized that greater solute mass present in these regions would ultimately lead to greater precipitate mass.

The work described here involved single-grain evaporation experiments, where the spatial distribution of precipitates formed following evaporation was observed through SEM imaging of thick precipitates, combined with Energy Dispersive X-ray Spectroscopy (EDS) to quantify the spatial distribution of thinner precipitates. A model of the evaporation-precipitation process was developed and used to assess the hypotheses of the work.

2.2 Materials and Methods

2.2.1 Materials

Sodium chloride (NaCl, MW=58.44 g/mol) and sucrose ($C_{12}H_{22}O_{11}$, MW=342.3 g/mol) were chosen for the study as representative high-solubility inorganic (sodium chloride) and

organic (sucrose) solutes. The solubilities of the compounds are approximately 26% w/w and 70% w/w for sodium chloride and sucrose, respectively. Experiments were conducted at 0.1 and 0.2 M for sodium chloride, and 0.05 and 0.1 M for sucrose. These concentrations correspond to approximately 2.2 and 4.4% of the solubilities of the two compounds.

2.2.2 Experimental Procedures

Sand grains used for experiments were taken from a beach sand sample collected from Sandwich, Massachusetts. The sand sample was initially washed in deionized water using a sonicator to agitate the grains to enhance cleaning and removal of loosely attached fines. Grains were air dried and then mounted on aluminum stubs with carbon tape for precipitation experiments and SEM imaging. All SEM images for the work were collected with the secondary electron detector of a Zeiss NEON 40 EsB high-resolution Scanning Electron Microscope (SEM). Energy Dispersive X-ray Spectroscopy (EDS) mapping was done using the same system. EDS mapping was used to identify regions containing carbon for samples with sucrose precipitates, and chloride for samples with sodium chloride precipitates. In order to allow multiple experiments to be conducted using the same grain, grains were not sputtered with gold alloy for imaging, to avoid modifying the surface properties of the grains.

Initial images of grains were taken prior to the start of experiments, and then experiments were conducted exploring precipitation patterns on grain surfaces. Experiments involved placing a drop of sodium chloride or sucrose solution on each grain, with a volume sufficient to just cover the grain, and then allowing it to air dry for at least twelve hours prior to SEM imaging and EDS mapping. After imaging, grains were cleaned by soaking in nanopore water for at least three hours, accompanied by gentle agitation. Grains were then air dried overnight, and the process was repeated with a new solution. Experiments were conducted in the following order:

0.1 M sucrose, 0.1 M sodium chloride, 0.05 M sucrose, 0.2 M sodium chloride.

2.2.3 Numerical Simulation

To better understand the precipitation process, a finite difference model was developed to simulate the evaporation of water films on sand grains, and the resulting water film flow and solute precipitation. The model begins with a three dimensional elevation map of the grain surface, calculated using a hybrid stereoscopic/shape-from-shading reconstruction method developed previously by the authors for extracting maximum detail from SEM images of geologic material surfaces (Yan *et al.*, 2017). The elevation map is then downsampled to a lower resolution (in this case to a resolution of approx. 110×80) for calculations.

The model works by calculating the theoretical shapes of capillary held water films on the sand grain over a range of specific capillary pressures using a method developed previously by the authors (Kibbey, 2013). (The lower resolution elevation map is needed to allow these computationally-expensive interface shape calculations.) A zero slope boundary condition around the perimeter of the elevation map is used for all calculations.

The process of placing a drop of solution on the grain is simulated by starting with water at a positive pressure (i.e., a negative capillary pressure), and then allowing pressure to decrease (capillary pressure to increase) as water evaporates. Water film profiles are calculated at 0.1 cm intervals at capillary pressures between -1 and 2.5 cm water, and then at 0.5 cm intervals from 2.5 to 20 cm water. Note that the smaller intervals at lower capillary pressures are necessary because a greater change in surface profile shape occurs with a given capillary pressure step at lower capillary pressures. The movement of solutes is simulated by assuming changes in water film configuration with capillary pressure results from evaporation. At each capillary pressure

step, all isolated regions within the water film are identified and considered separately. Isolated regions are defined by the thickness of films, in that regions where capillary films are not present (i.e., only adsorbed films are present) are assumed to not transmit water in the timescale of experiments.

According to Langmuir's evaporation equation, the evaporation rates of the same surface areas are equal under the same conditions. As such, the total evaporation between steps for all cells in a given region will be equal, except for cells which evaporate to dryness between steps. The amount of water loss due to evaporation at each cell within each isolated region is determined through Eq. 2.1 as follows.

$$\sum_{i,j\in A}(T_{i,j}^{k+1} - T_{i,j}^{k}) = \sum_{i,j\in A} E_{i,j} = E_{totA} \tag{2.1}$$

Where $T_{i,j}^{k}$ is film thickness at cell *i,j* at step *k*, and the sums are over all points in isolated region A. $E_{i,j}$ is the amount of fluid evaporated from cell *i,j* between step *k* to *k*+1. For all cells where $T_{i,j}^{k+1} > 0$, $E_{i,j}$ has the same value within the region; For cells where $T_{i,j}^{k+1} = 0$, $E_{i,j}$ is taken to be $T_{i,j}^{k}$. Based on these conditions, Eq. 2.1 is used determine values of $E_{i,j}$ at each point in region A.

Following evaporation at each step, concentrations are updated locally and precipitation allowed to occur if concentration exceeds the solubility. Two dimensional flow within the region is then simulated by implicitly solving the mass balance on water entering and leaving cells needed to produce a water surface that matches the surface defined by $T_{i,j}^{k+1}$. Water is

allowed to flow between cells within each isolated region, with flow into and out of each cell determined by implicit solution of the global mass balance for the region. Once velocities have been determined from the water mass balance, a mass balance on the solute is used to calculate transport between cells within each isolated region over the pressure step.

2.3 Results and Discussion

The two sand grains use in this study are shown in Figure 2.1. Each of the studied grains is approx. 1 mm in width. Based on EDS measurements, both are primarily quartz sand. Ridges on Grain A (Fig. 2.1A) are slightly more rounded than ridges on Grain B (Fig. 2.1B), but both grains exhibit distinct edges and surface striations, as well as relatively smooth regions between ridges.

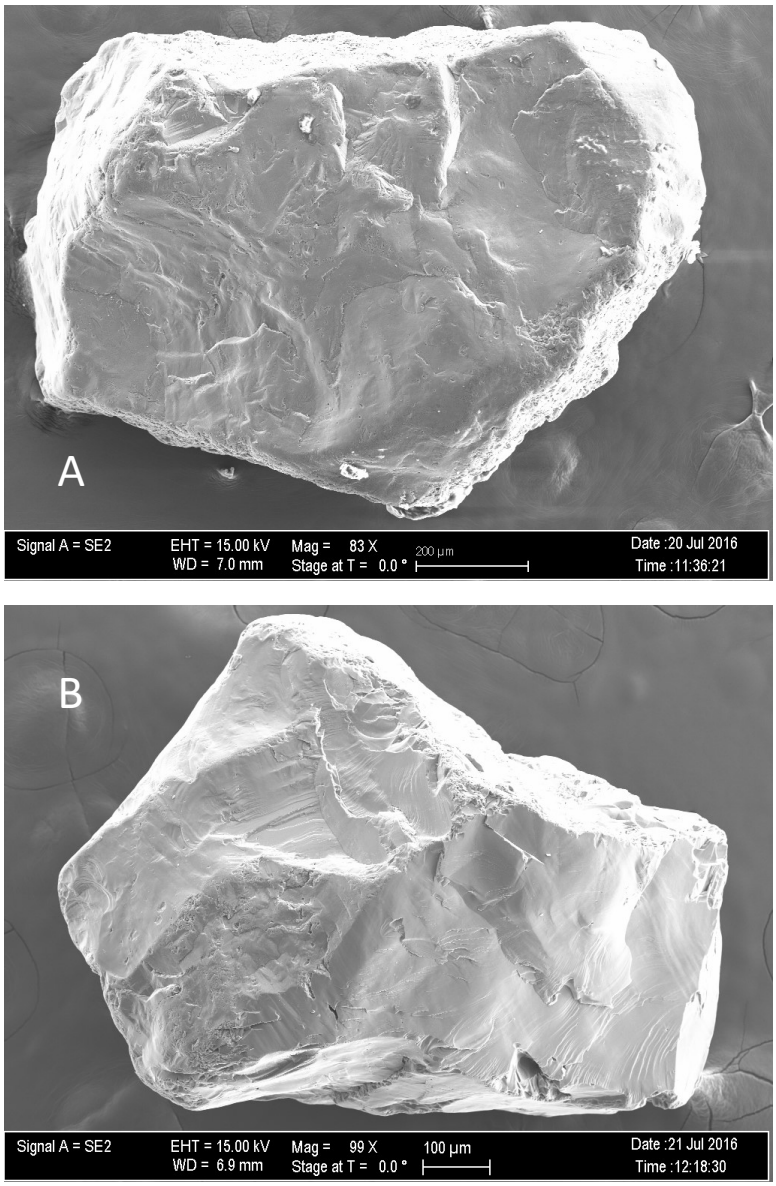


Figure 2.1. SEM images of the two quartz sand grains used in the study, Grains A and B.

Figure 2.2 shows renderings created from three-dimensional elevation maps of the top surfaces two grains, further illustrating the topography of the grains. (Note that the reconstruction method is based on stereoscopic and shape-from-shading computations from two images taken at different angles (Yan *et al.*, 2017), so is only able to reconstruct elevations of one side of a grain.)

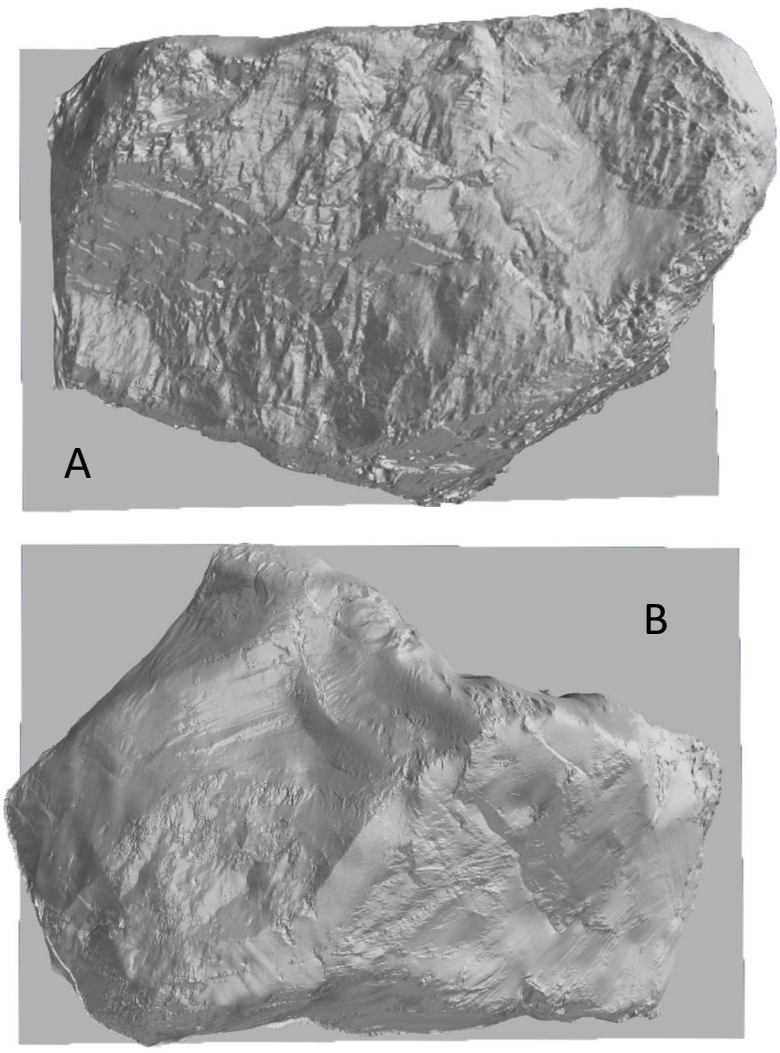


Figure 2.2. Calculated high resolution elevation maps for Grains A and B.

Figures 2.3 and 2.4 show precipitation of the two solutes on the two grains. Figure 2.3 corresponds to Grain A, while Figure 2.4 corresponds to Grain B. Images on the left side of each figure show SEM images of the grains with sodium chloride (Figures 2.3A, B and 2.4A, B) and sucrose (Figures 2.3C, D and 2.4C, D). Images on the right side of the figure add superimposed EDS maps, showing the locations of sodium chloride and sucrose precipitates. (It should be

noted that some precipitates in low regions on the left sides of grains are not apparent in EDS maps, as a result of shadowing and the geometry of the detection system.)

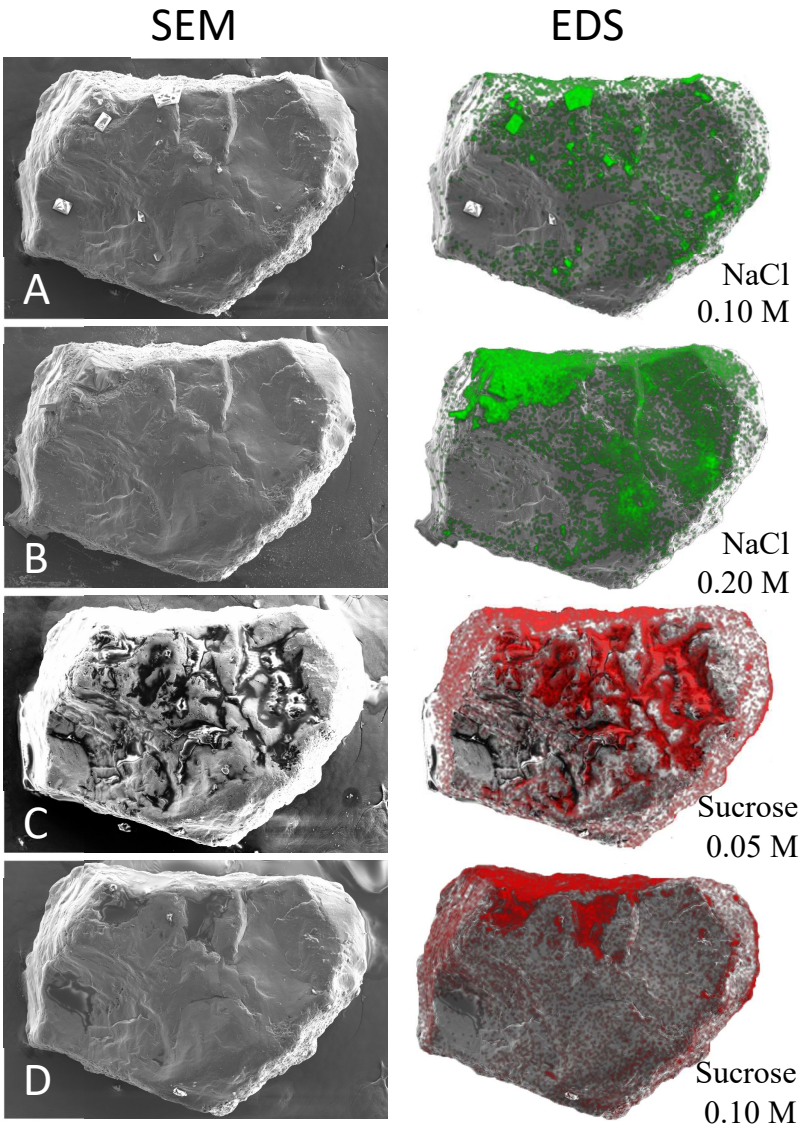


Figure 2.3. Precipitation of sodium chloride (A, B) and sucrose (C, D) on Grain A. SEM images are shown at left, while images with EDS overlays are shown at right.

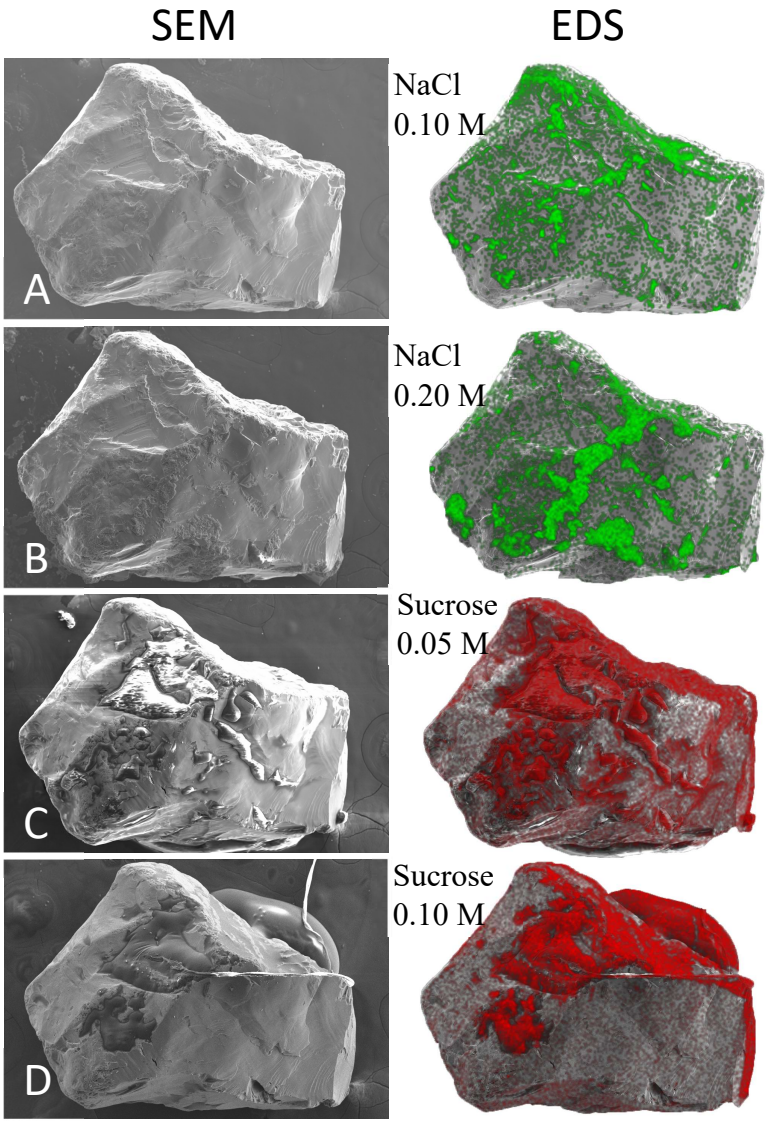


Figure 2.4. Precipitation of sodium chloride (A, B) and sucrose (C, D) on Grain B. SEM images are shown at left, while images with EDS overlays are shown at right.

In the SEM images, sodium chloride can be observed in the form of large, distinct crystals on the grains, while sucrose can be observed in more amorphous, blob-like configurations. It should be noted that it is probable that the sucrose may still be partially gel-like in these images; subsequent tests on flat surfaces found that dried sucrose remained sticky for several days before eventually crystallizing. The reason for this is likely the extremely high viscosity of sucrose solutions near their solubility (e.g. more than 200 cP), a situation which likely significantly decreases the rate of water diffusion out of the drying phase. Regardless, the high viscosities of sucrose gels also means that the observed locations of sucrose on the grains in Figures 2.3 and 2.4 should be representative of their likely final locations after crystallization, since further flow would be unlikely.

Three major features are notable from examination of Figures 2.3 and 2.4. First, examination of the superimposed EDS maps shows that both solutes are present over much of the grains, regardless of topography. Although regions of greater precipitate thickness are noted (and in many cases observable in the SEM images), low thickness precipitate is widely present over the surfaces of grains. One implication of this is that mass transfer during subsequent dissolution might initially be high because of the large precipitate surface area from low-thickness precipitates, but might decrease early in the dissolution process as low-thickness precipitates are dissolved from the surface, leaving only localized thicker precipitates.

Second, it is apparent from the figures that the location and coverage of high thickness precipitates does not necessarily correlate well with the initial concentration for either solute. For example, on both grains the 0.05 M sucrose samples appear to have greater coverage of high thickness sucrose (i.e., black blobs in the left subfigures, dark red in the right subfigures). The reason for this is likely that ultimate precipitation patterns are very sensitive to starting

configuration of fluid on grains, so slightly different placement of droplets of solution can yield very different precipitate patterns. Note also that in some cases, precipitate forms around the edges of grains, as water initially on the grains flows onto the surrounding support during evaporation.

Finally, perhaps the most important observation that can be made from Figures 2.3 and 2.4 is that the hypothesis of the work – that thick precipitates would be concentrated in low regions of grains – appears to be largely correct for the sucrose, but *not* for the sodium chloride. Examination of the figures shows that while the greatest masses of sucrose precipitates are present in low regions on grain surfaces, the bulk of thick sodium chloride precipitates are present on *edges* surrounding low regions.

In order to understand the differences between the behaviors of the two solutes, it is useful to first consider the behavior of the sodium chloride. Figure 2.5 shows a simulation of the 0.2 M sodium chloride on Grain B, based on the model described Section 2.2 (Numerical Simulation). Interestingly, the model predicts that the greatest mass of sodium chloride precipitates will be along edges rather than on valleys, just as is observed in Figures 2.3 and 2.4.

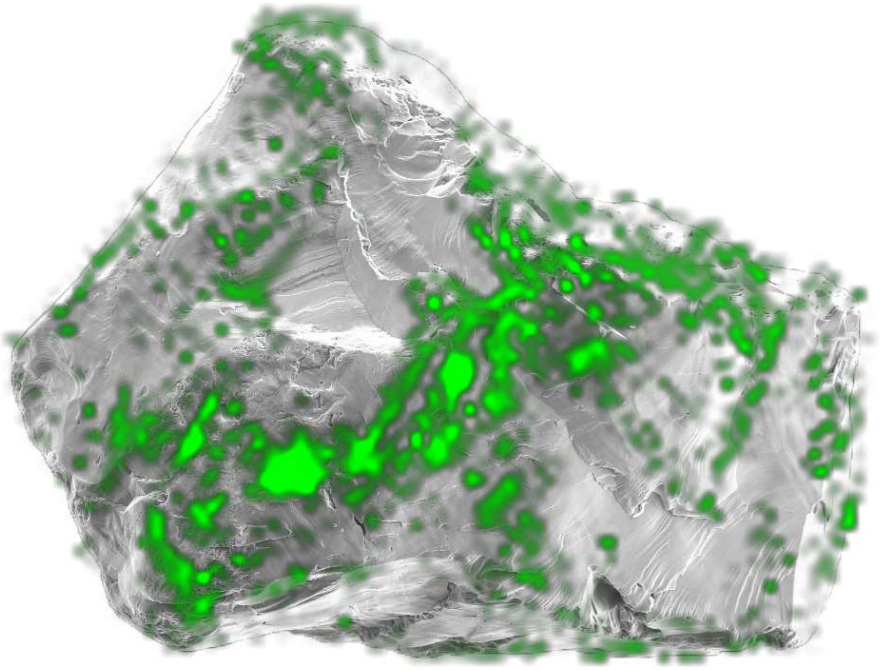


Figure 2.5. Model-simulated precipitation of sodium chloride (0.2 M) on Grain B.

The source of this behavior is illustrated in Figure 2.6, which provides a schematic explaining the hydraulics of water redistribution that accompanies evaporation. When an isolated fluid evaporates on a rough surface, the evaporation process is accompanied by an increase in capillary pressure (a decrease in radius of curvature). That is, the water surface goes from line 1 to line 2 in Fig. 2.6A.

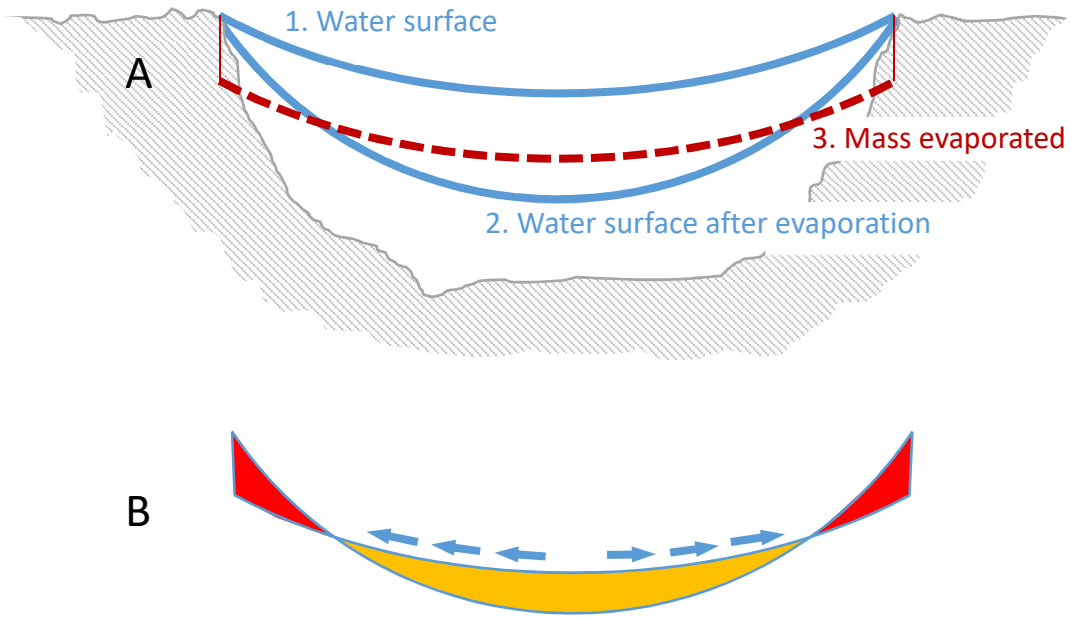


Figure 2.6. Schematic illustrating the source of currents in water films during evaporation.

This behavior is widely observed and is the result of partial interface pinning on rough surfaces; even if the edges of isolated water film recede during evaporation (as is often observed), pinning causes the process to be accompanied by curvature change. (Interestingly, note that the same behavior has been observed for long term dissolution of liquid drops on solid surfaces, where drop pinning causes long term changes in surface curvature (Mohammad & Kibbey, 2005)). Water redistribution during evaporation comes from a mismatch between the spatial evaporative demand and the change in water volume required to reach the new water configuration. As discussed in Section 2.2, the Langmuir evaporation equation indicates that evaporation rates should be the same across the water surface. In Fig. 2.6A, line 3 indicates what the water surface would be if uniform evaporation were occurring everywhere, in the absence of capillary pressure changes, i.e., the water surface would shift downward parallel to the original surface. Figure 2.6B illustrates the source of the flow, as water must continuously flow from the yellow region to the red region to achieve the final water surface configuration.

Figure 2.7 both illustrates this behavior in a model system, and also provides clues to the differences between sucrose and sodium chloride. The figure shows precipitation on a glass slide from drops of two high concentration (approx. 20% w/w) solutions, one (Fig. 2.7A) containing sucrose, the other (Fig. 2.7B) containing sodium chloride. Note that the sodium chloride (Fig. 2.7B) forms a ring of crystals around the edges of the droplet. Once precipitation begins at seed crystals near the edges of the drop, flow from the center of the drop feeds the crystals as evaporation continues. In the case of sucrose (Fig. 2.7A), note that while the droplet largely retains its initial outline, the center of the drop is depressed compared to the edges. The depression in the center is due to the radial water flow during evaporation. The fact that the footprint of the drop remains largely unchanged in this case, however, is largely the result of the

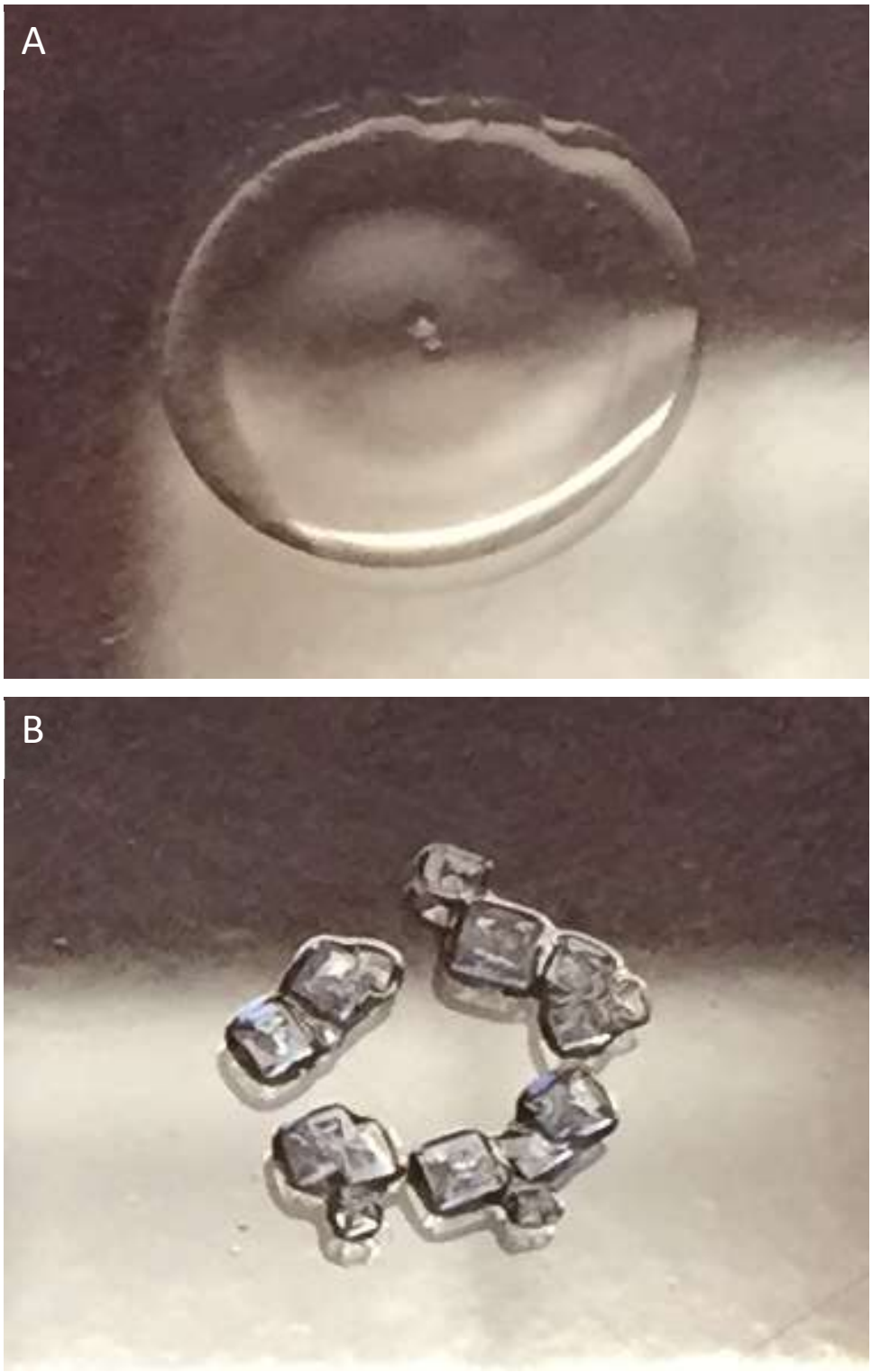


Figure 2.7. Precipitation of sucrose (A) and sodium chloride (B) from high concentration solutions on glass microscope slides.

very different viscosity behavior of sucrose and sodium chloride near their solubilities. While the viscosity of sodium chloride near its solubility is only about twice that of water (~2 cP), the viscosity of sucrose near its solubility is about two hundred times that of water (~200 cP). As such, when the concentration is reached where sodium chloride can precipitate, the surrounding fluid remains quite mobile. In contrast, sucrose becomes increasingly immobile as its solubility is approached. It is likely that this difference also results in the sucrose precipitation behavior found in Figures 2.3 and 2.4.

Because the model described in Sec. 2.2 does not include viscosity effects, simulation of sucrose based on that model produces behavior not unlike that in Figure 2.5 (sodium chloride), where precipitates are on edges – a result inconsistent with experimental results in Figure 2.3 and 2.4. As such, the model was modified in an effort to approximate the behavior of sucrose. The modification caused all solutes in a cell where precipitation occurred to be immobilized (approximating the effects of high viscosity), and allowed precipitates to delineate isolated regions, preventing transport. Essentially, once precipitation occurred at some point on a grain, it would block the movement of solutes past that point. The result is that solutes become isolated in low regions, and are not able to flow to edges. Figure 2.8 shows the modified model applied to simulating precipitation of 0.05 M sucrose on Grain B. Note that precipitate is largely present in valleys on the grain, a result that is largely consistent with experimental observations.

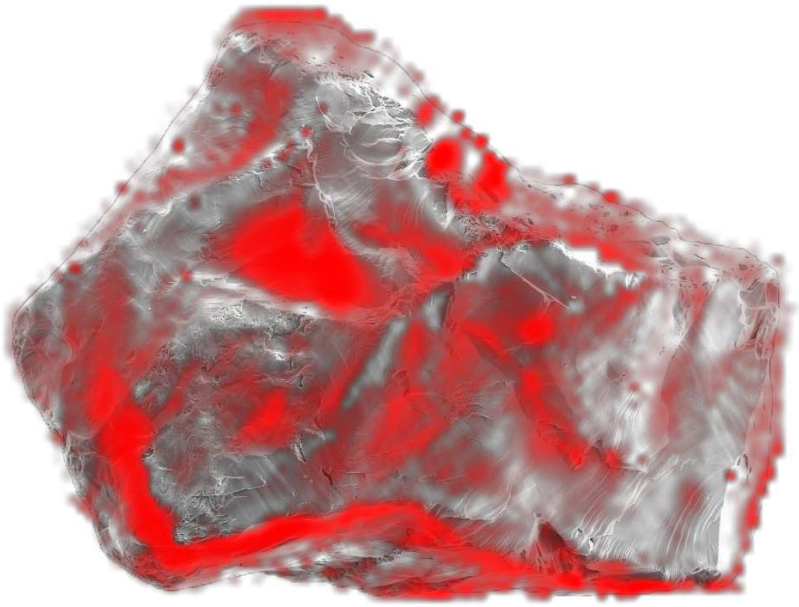


Figure 2.8. Model-simulated precipitation of sucrose (0.05 M) on Grain B, calculated based on the revised model that includes viscosity effects.

2.4 Conclusions

The hypothesis of this work was that precipitates would be concentrated in low points on solid grains, due to solutes concentrating and precipitating in receding water films. The results of this work suggest that that hypothesis is generally incorrect. While the expected behavior was observed for experiments with sucrose, it was not observed for experiments with sodium chloride. In sodium chloride experiments, precipitation was found to occur at ridges surrounding low points. This result is likely the result of water movement on grain surfaces induced by evaporation, where water flows from valleys to surrounding ridges as evaporation occurs; while the water film does recede into the valleys, in the sense that it remains thickest there after

continued evaporation, the receding process is accompanied by significant hydraulic gradients toward the ridges. In the case of sucrose, the very high viscosity at its solubility likely results in trapping of solutes in valleys. Numerical simulations were able to duplicate both of these effects.

Considering the behaviors and physical properties of the two solutes studied, it is likely that the behavior of sodium chloride (i.e., precipitation on ridges) is likely to be the far more common among other solutes, because the high viscosity at solubility for sucrose which causes its precipitation behavior results primarily from its extremely high water solubility (~70% w/w). Solutes with lower solubilities and accompanying lower viscosities at solubility would be expected to form concentrated precipitates on ridges, as was observed for sodium chloride.

Chapter 3

The Relationship Between Microscopic Grain Surface Structure and the Dynamic Capillary-Driven Advance of Water Films over Individual Dry Natural Sand Grains

Abstract

The transport in water films in the vadose zone is a subject of continued interest, because information about how water films behave at the grain scale could potentially improve our understanding of transport at a larger scale. This work explores how the microscopic surface structure of a sand grain affects the pattern of water being wicked onto its surface when it is initially dry. Experiments were carried out using water dyed with Sulforhodamine B. The dyed water was allowed to move over initially-dry individual grain surfaces under the influence of capillary forces alone, and an optical microscope was used to monitor the patterns of liquid on the grain surfaces over time. Results showed that roughness in the form of micro pores is likely required for rapid wicking to occur on individual grains, although some rough grains with limited micro-porosity did exhibit wicking. For grains which exhibited wicking, patterns of wicking tended to follow areas where greater roughness was identified. However, roughness alone was not found to be a sufficient predictor of whether wicking will occur on a grain surface, or how velocity will vary between different grains.

3.1 Introduction

Movement of water films is important in unsaturated media for a range of phenomena ranging from drainage to mass transport. One important case is the situation where water encounters a dry surface and is pulled along by capillary forces. This phenomenon could be

important, for example, when a liquid contaminant spill occurs onto an initially dry soil. The purpose of this work was to study how surface roughness on individual grain surfaces influences patterns of water movement at the grain surface scale.

Spreading refers to the spontaneous movement of liquid over a solid surface as a result of a zero or positive spreading coefficient (Eq. 3.1).

$$S_{L/S} = W_{LS} - W_{LL} = \gamma_{SV} - \gamma_{LV} - \gamma_{SL} \tag{3.1}$$

Where $S_{L/S}$ is the spreading coefficient for spreading of a liquid, W_{LS} is the work of adhesion (energy required to separate a unit area of liquid from solid), and W_{LL} is the work of cohesion (energy required to separate a unit area of liquid from another unit area of liquid), and γ_{SV}, γ_{LV} and γ_{SL} are surface energies between different surfaces. Combining Eq. 3.1 with the Young equation gives the form of the spreading coefficient for a solid surface (Eq. 3.2):

$$S_{L/S} = \gamma_{LV}(\cos\theta - 1) \tag{3.2}$$

From Eq. 3.2, it can be seen that $S_{L/S}$ can never be positive, and can only be zero if the contact angle, θ, is zero. Figure 3.1 shows a drop of liquid on a flat solid surface, with the corresponding surface energies. For the drop to spread on the surface, the contact angle must be zero.

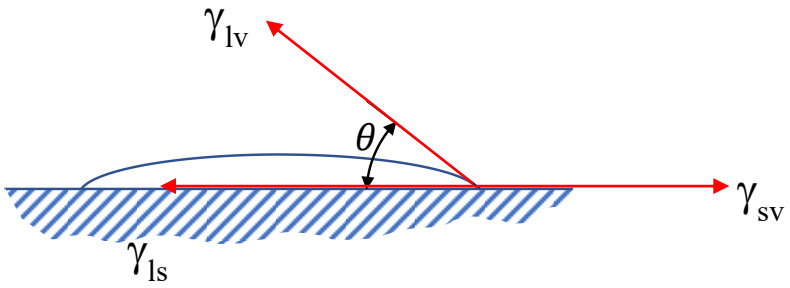


Figure 3.1. Schematic showing the contact angle and the surface energies acting on the contact line for a drop of liquid on a solid surface exposed to vapor phase.

On rough surfaces, in addition to liquids spreading due to a zero spreading coefficient, liquids can also be pulled along grooves or through micropores on the grain surface by capillary forces. This is referred to as wicking. Figure 3.2 is a schematic showing how liquid can be pulled into a surface groove.

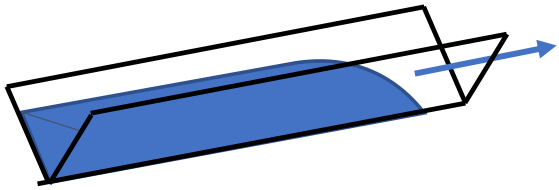


Figure 3.2. Figure showing the process of liquid being wicked along a surface groove.

Several studies have been carried out which studied the relationship between roughness of a surface and capillary driven wicking (Oliver & Mason, 1977, 1980; Cazabat & Stuart, 1986; Bico *et al.*, 2001; McHale *et al.*, 2004; Ishino *et al.*, 2007; Chen *et al.*, 2009; Vorobyev & Guo, 2010; Quan Lai *et al.*, 2013; Lai *et al.*, 2014; Iwamatsu, 2017). The Washburn Law indicates that a wetting front advances as the square root of time, and has been found to hold true for rough surfaces as well as for wicking by porous media (Ishino *et al.*, 2007; Chen *et al.*, 2009; Cheng *et al.*, 2015).

Many of these studies were carried out on liquid spreading under positive pressure (Oliver & Mason, 1977, 1980; Cazabat & Stuart, 1986; Quan Lai *et al.*, 2013; Lai *et al.*, 2014) whereas in the unsaturated zone of a porous medium, liquid is under negative pressure. While some studies have examined liquid wicking under negative pressure, many of the surfaces studies were artificially created fractals with repeating surface texture patterns not necessarily comparable to natural sand grain surfaces (Ishino *et al.*, 2007; Chen *et al.*, 2009; Vorobyev & Guo, 2010). Studies have shown that the wicking of liquids in porous rock is due to capillarity within connected pores and spreading on the rough surfaces of fractures in the rock (Cheng *et al.*, 2015)

3.1.1 Movement of capillary films over rough surfaces

In an unsaturated soil, the pores are filled partly by water and partly by air. The water is held under negative pressure in connected pores between soil grains, and as water films on grain surfaces (Tuller & Or, 2005; Kibbey, 2013). Until recently, water films were largely believed to be very thin and immobile in the liquid phase. Recent research (Kibbey, 2013) has shown that

these films could be orders of magnitude thicker than once thought and could potentially contribute significantly to transport in the liquid phase. Various studies have explored the movement of water under negative pressure through soil pores (Rhoades *et al.*, 2015; Hird & Bolton, 2017) and rock fractures (Tokunaga & Wan, 1997; Cheng *et al.*, 2015; Yang *et al.*, 2016) but little work has been reported on the movement of films across the surface of individual natural sand grains.

3.1.2 Objectives

This study aims to explore the relationship between surface roughness of a grain and the pattern and velocity of water being wicked across its surface when initially dry. The hypothesis driving this work was that the patterns and velocities of water wicking onto initially dry grain surfaces would be dictated by the roughness of the grain surface. In other words, the roughness of a grain surface will enhance the wicking of capillary films across the grain surface while smoother surfaces will experience less wicking. This is expected for two reasons. The first reason is that roughness of a hydrophilic surface has been shown to further reduce low contact angles of drops of water on those surfaces liquids thus enhancing wetting (McHale *et al.*, 2004). Most natural sand grains are hydrophilic (assuming they are not coated by some low energy contaminants like oils), so it is expected that the roughness will further enhance wetting of the grain surfaces. Second, the surface of many sand grains is covered with smaller scale grooves, fractures or pores which can draw in water through capillary forces thus increasing spread (Ishino *et al.*, 2007; Vorobyev & Guo, 2010).

In this work, surface structure was explored with scanning electron microscope (SEM) imaging and edge detection, while wicking patterns on various grains were studied using optical microscopy. Humidity was controlled in selected experiments to understand the impact of evaporation on flow patterns and rates.

3.2 Materials and Methods

3.2.1 Materials

The sand sample used for this work was an ASTM C33 concrete sand which means it meets ASTM guidelines for use as concrete aggregate. It has a d_{50} of 1.18mm. The sand sample was washed several times in deionized water with the aid of a sonicator wand until the water was clear. The sand was then air dried.

Grains were initially selected at random from the sample. Initial experiments on a few of the selected grains revealed that smoother grains didn't show any signs of wicking while rougher grains did. Four rough grains were selected for further experiments. The grains are referred to as grains 1, 2, 3 and 4 in this chapter. Details of the specific grains are given as they are presented.

The selected grains were imaged using the secondary electron detector of a Zeiss Neon 40 EsB Scanning Electron Microscope (SEM). In preparing the grains for the microscope, the grains were mounted on aluminum stubs using carbon tape. The grains were not sputter coated to preserve the surface structure for subsequent wicking experiments. The individual grains were then removed from the carbon tape, mounted on glass slides using a two-part epoxy glue and allowed to set for 24 hours at room temperature before performing flow experiments.

Sulforhodamine B dye, a conservative tracer, was used in water to highlight the path of flow in the wicking experiments. A concentration of approx. 0.200 g/l (~$2x10^{-4}$ % w/w) was used to make it easy to observe thin films of water.

3.2.2 Experimental Procedures

The wicking experiment was set up using a section of 31 gauge stainless steel hypodermic tubing. One end of the tubing was placed against the grain surface, while the other end was immersed in an open reservoir containing dyed water. The reservoir was placed with the liquid surface approx. 1 cm below the grain surface, to exert a capillary pressure on the dyed water wicking onto the grain surface through the steel tubing. (The use of hypodermic tubing caused water to be pulled up from the reservoir to the grain through capillary forces.)

Kissa (1996) classified the wicking process into two groups based on the volume of reservoir the wicking occurs from. The first group is wicking from an infinite reservoir while the second is wicking from a finite reservoir. The inlet tubing for the experiments was in contact with the surface of the grain all through the wicking experiments in this work simulating an infinite reservoir.

A schematic of the experimental setup is shown in Figure 3.3. The grains were initially dry before the experiment was started. An optical light inspection microscope was used to capture time lapse images of the grain to observe the pattern of the wicking dyed water. The effect of humidity was also explored by performing selected experiments in a humidity-controlled enclosure. The enclosure prevented air from moving in or out of the immediate surroundings of the grain. Additional water droplets were placed around the grain within the

enclosure to provide a source for water to maintain the humidity in the enclosure. A relative humidity meter was positioned within the enclosure to monitor humidity changes. Experiments carried out in the enclosure were at relative humidity ranging between 80 and 97%. Those carried out in the open air had relative humidity vary between 10 – 16%.

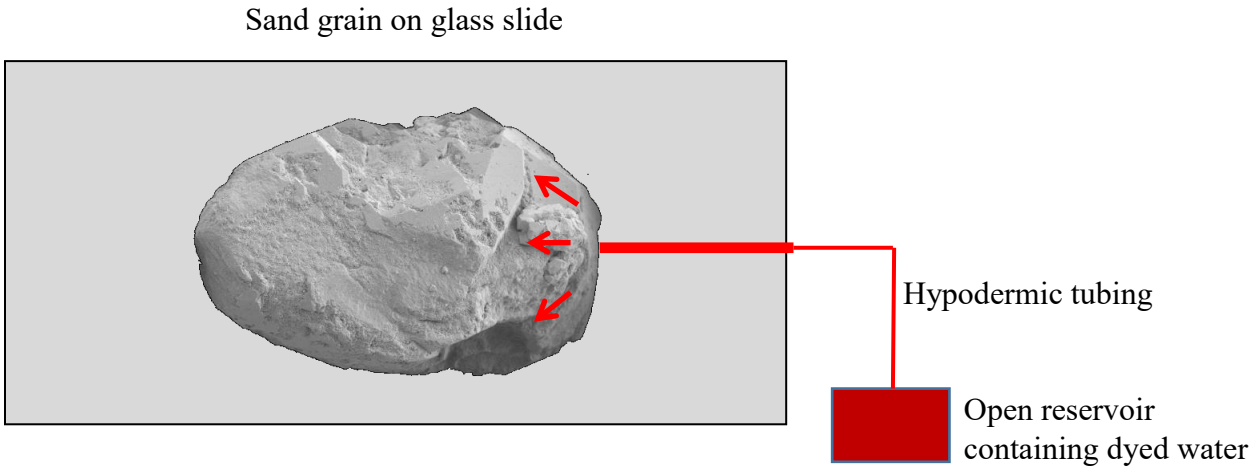


Figure 3.3. Schematic of the experimental setup showing reservoir containing dyed water connected by a hypodermic tubing to contact the grain.

After each wicking experiment, the dye was washed off the grain by soaking it in methanol. In cases where the stains didn't come off with methanol, the grains were soaked in 30 % v/v acetic acid to remove the stains. The grains were then rinsed in water extensively and allowed to air dry for the next experiment.

3.2.3 Image Processing

A numerical code was written in Python to process the SEM images and generate edge density maps from them. The code normalized SEM images by intensity first. It then utilized the

Sobel edge detection algorithm to highlight edges on the SEM images. The Sobel algorithm is an image processing filter which is used to emphasize the edges on an image. The resulting edge map was smoothed using a moving square averaging method to generate an edge density map showing the average density of edges over the surface on the grain. Fiji software was also used in image processing (Schindelin *et al.*, 2012). Wicking patterns on the grains were studied to determine if the edge density map could give an indication of the pattern and/or rate of wicking expected at different points on the grain.

3.3 Results and Discussion

Figure 3.4 shows images of Grain 1 in this study. The grain is a highly rough grain, with dimensions of approx. 4250 µm × 2700 µm. Figure 3.4A shows an SEM image of the grain, Figure 3.4B shows the edge map of the grain, while Figure 3.4C shows the filtered edge density map. The filtered edge density map is brightest in the regions that have the highest densities of roughness features, as indicated by optically-observed edges on the surface. To observe how change in roughness over the surface of a single grain affected wicking, the contact point on grain 1 was varied, going around the grain in a counterclockwise direction to study how rate of wicking changed over different portions of the grain surface with different roughness. The initial velocity of wicking was calculated by dividing the measured extent of wetting front from inlet point with the time taken to reach that extent. The measured extent was taken to be the longest distance the dye spread away from the inlet tubing early in the wicking period. The positions on the grain surface were designated from an arbitrary origin on the grain in a counterclockwise direction. The wicking experiment was carried out with each position serving as contact point for the inlet tubing. The points were numbered 1 to 9 beginning from the chosen origin and moving in a counterclockwise direction.

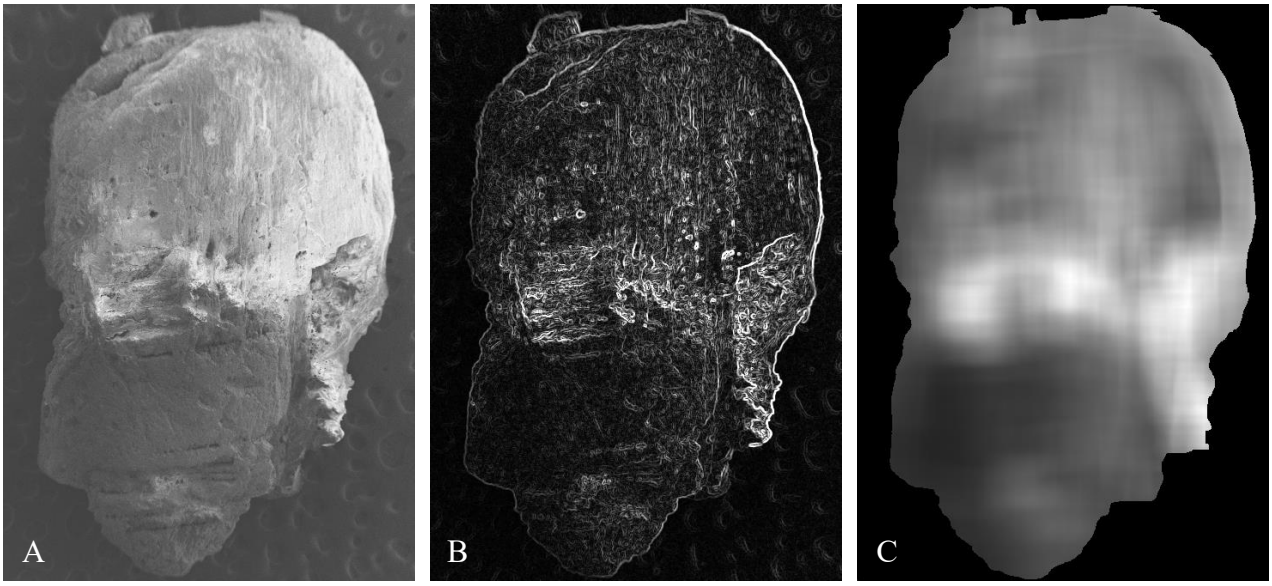


Figure 3.4. Images of Grain 1: A. SEM image. B. Edge map. C. Filtered edge density map.

Figure 3.5 shows images of the flow observed when the inlet tube was placed at point 1 on Grain 1. The images were captured at 5 second intervals. Flow moved from point 1 on the grain to point 6 in about 25 seconds.

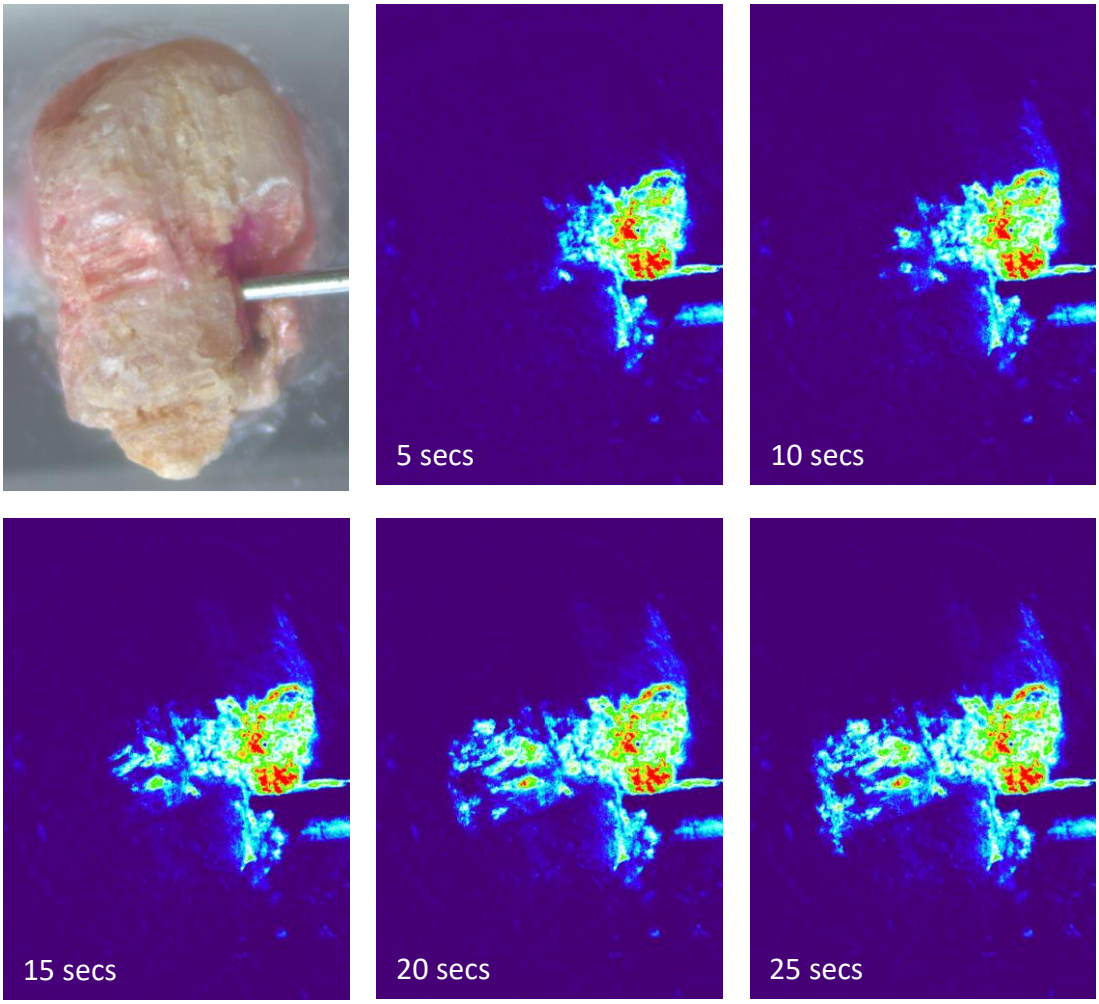


Figure 3.5. Images showing flow of dyed water across Grain 1

Figure 3.6 shows the designated inlet positions on grain 1. The plot in Figure 3.7 shows the initial wicking velocities observed at the various inlet positions shown in Figure 3.6. For each inlet position, about 2 to 4 flow experiments were carried out. Figure 3.7 shows the maximum, minimum and average initial wicking velocities observed at each inlet position. The plot shows significant variation in the measured initial wicking velocities for each of the flow experiments carried out for any given inlet position. This points to the sensitivity of the experiments to exact starting position.

A plot of edge densities versus distance along path was made and superimposed on the plot in Figure 3.7 (plot of initial wicking velocity against distance along path). The superimposed plot is shown in Figure 3.8 and it shows a direct correlation between edge density and initial wicking velocities. Generally, the points on the grain with higher observed initial wicking velocities had higher edge densities. Although the relationship is not perfect, the fact that the two sets of data follow similar trends strongly suggests that roughness, as indicated by the edge density, is a reasonable predictor of the initial wicking velocity on an individual sand grain.

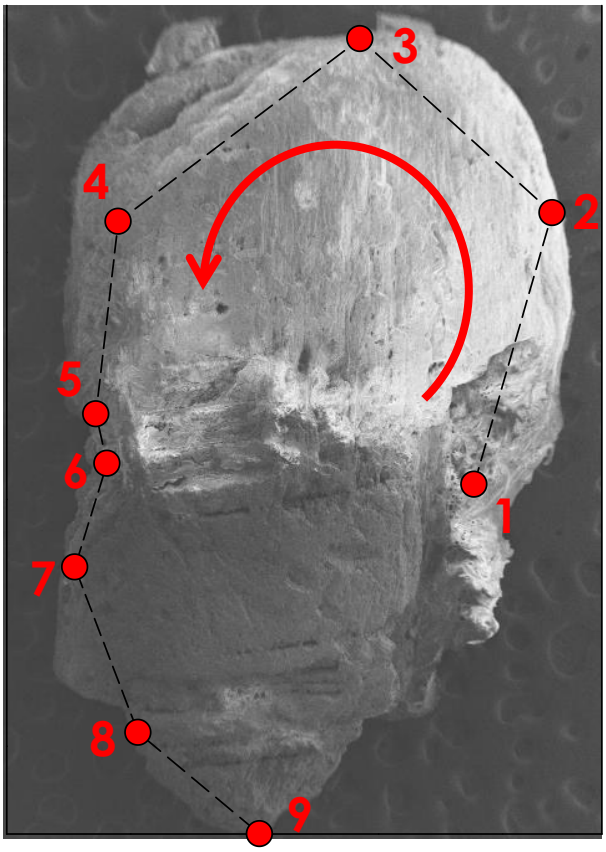


Figure 3.6. Inlet positions on Grain 1, numbered from 1 to 9

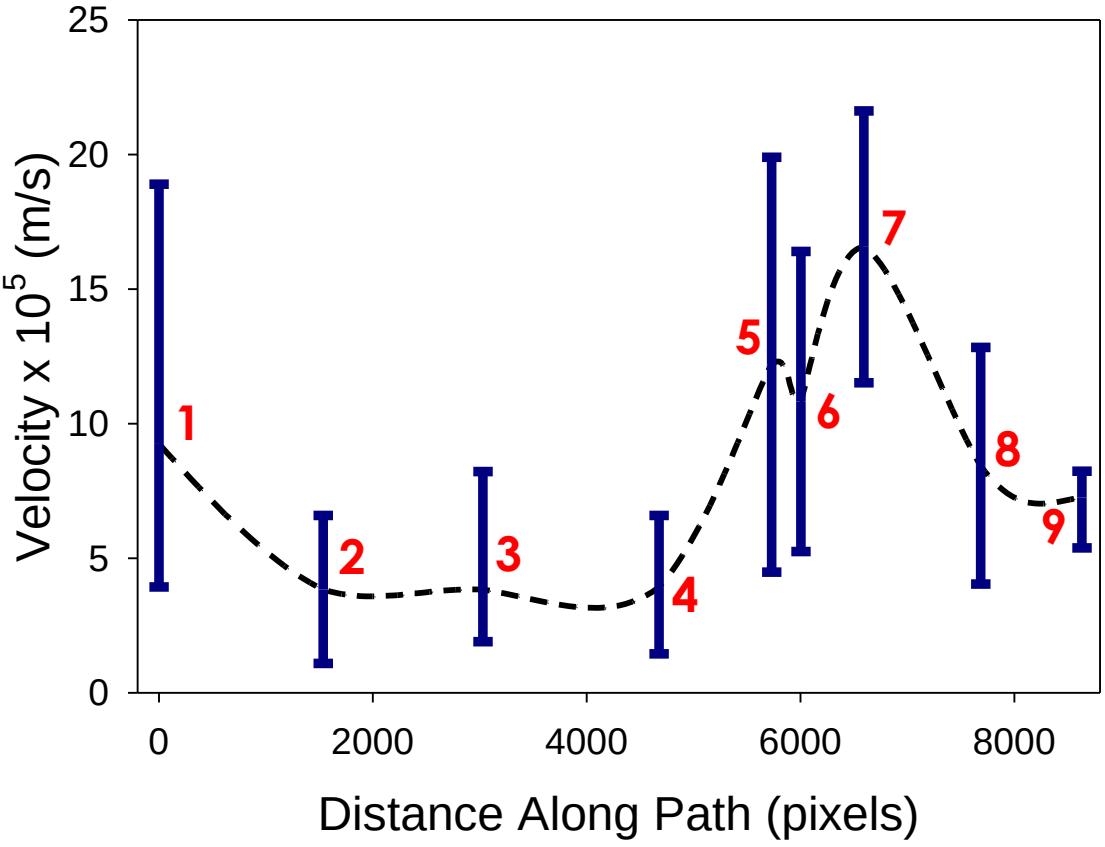


Figure 3.7. Plot of initial wicking velocity versus distance along path for points 1 through 9 showing minimum, maximum and average initial wicking velocities of the flow experiments at that point.

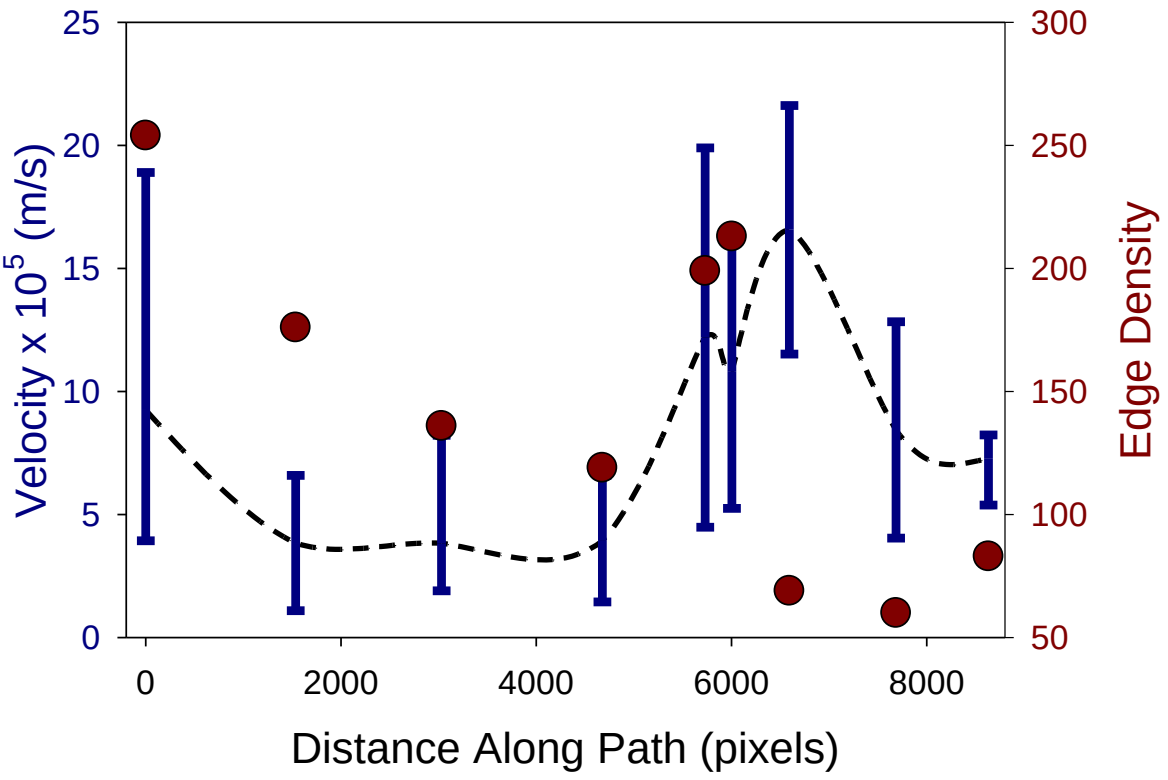


Figure 3.8. Plot of edge density versus distance along path superimposed on a plot of initial wicking velocity versus distance along path for points 1 through 9. Plot shows minimum, maximum and average initial wicking velocities observed during flow experiments at that point and the measured edge density of the inlet position.

Positions 1, 5, 6, 7 and 8 in Fig. 3.8 show relatively higher initial wicking velocities than the other positions. The common pattern that can be seen with these points is that the inlet tube is positioned around the roughest part of the grain. This allows wicking to immediately begin with thicker films and hence faster rates. Points 2, 3 and 4 are positioned at smoother portions of the grain and even though the liquid is wicked towards the rougher parts of the grain, the thinner films slow down the initial wicking velocity significantly. Point 9 is located on a rough portion of the grain from visual observation. The low observed initial wicking velocity at point 9 could be due to the position of the inlet tubing relative to the apparent direction of the roughness. The water is forced to wick at right angles to the direction of the grooves forming the roughness at point 9. At points 1, 5, 6 and 7, the inlet tubing is positioned parallel or nearly parallel to the direction of the grooves forming the roughness at those points thus allowing capillarity to help in pulling the water out of the tube into the grooves at a higher initial velocity.

Figure 3.9 shows images of Grain 2, a rough grain, approx. 3.7mm by 3.6mm, which also exhibited wicking. Figure 3.9A is an SEM image of Grain 2. Figure 3.9B shows the edge map of Grain 2 while Figure 3.9C is a filtered edge density map of Grain 2.

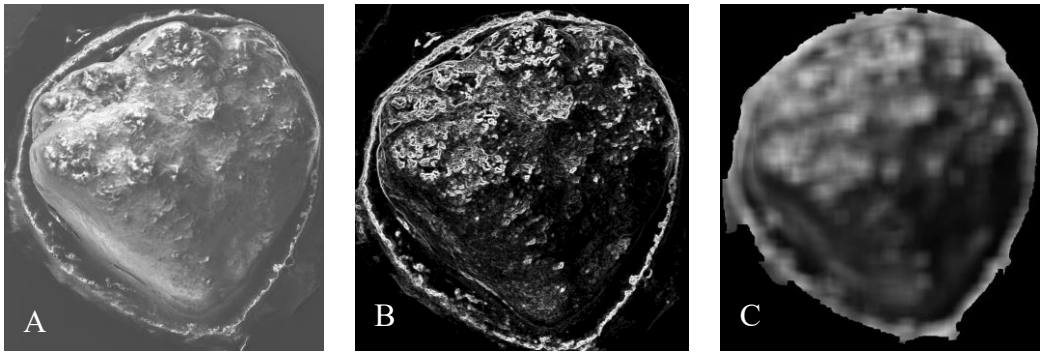


Figure 3.9. Images of Grain 2: A. SEM image. B. Edge map. C. Filtered edge density map.

Figure 3.10 shows the observed wicking on Grain 2. The images were taken at 2 minute intervals. Common to both Grain 1 and 2 is the tendency of the wicking to occur on the roughest parts of the grains. Figure 3.11 shows a side by side comparison of the filtered edge density plots and observed wicking pattern for both grains. There is some similarity between the wicking patterns and the filtered edge maps, in that the water flow tended to follow the roughest portions of the grain surfaces, as indicated by high spatial density of edges.

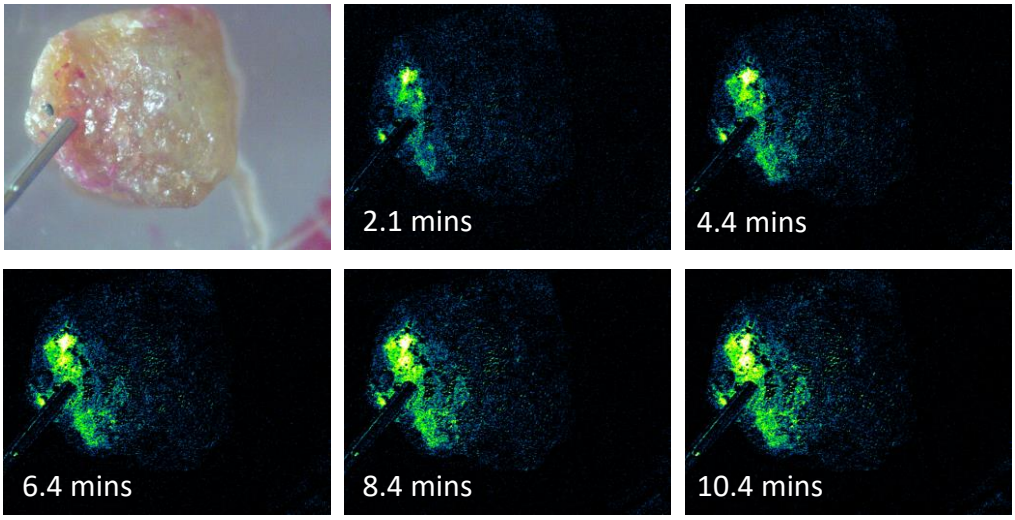


Figure 3.10. Images showing flow of dyed water across Grain 2

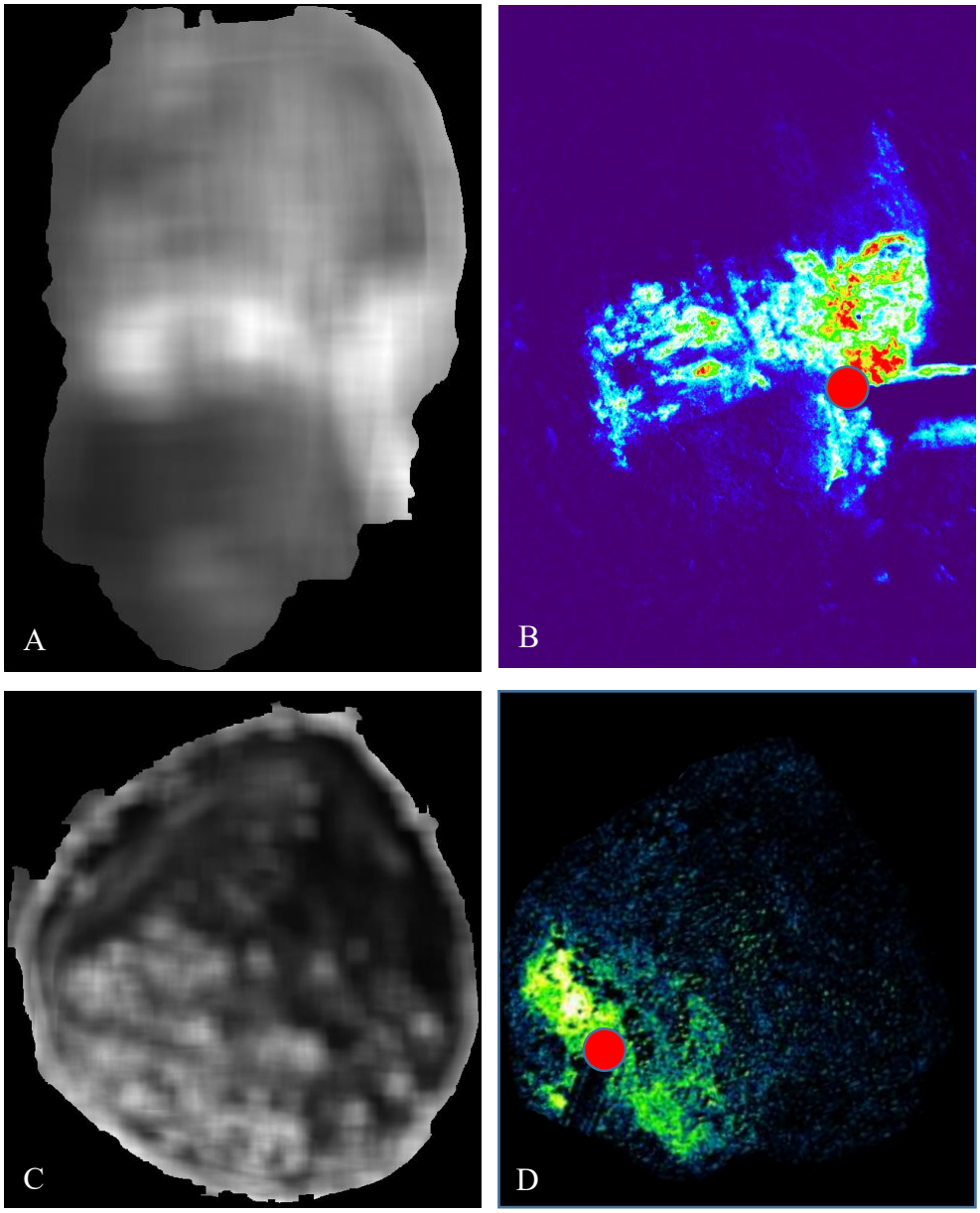


Figure 3.11. Images showing side by side comparisons of the edge density maps with the observed wicking pattern for Grains 1 and 2. The red dots indicate where the wicking started: A. Filtered edge density map for Grain 1. B. Observed wicking pattern on Grain 1. C. Filtered edge density map for Grain 2. D. Observed wicking pattern on Grain 2.

Although the patterns of wicking tend to follow surface roughness, it is important to note that wicking velocity differed widely between different grains, and some seemingly rough grains exhibited little or no wicking at all. For example, Figures 3.12 and 3.13 show images of two

additional selected grains, Grain 3 and Grain 4, which although they seemed rough, did not show any sign of flow either in open air, or in the humidity-controlled enclosure.

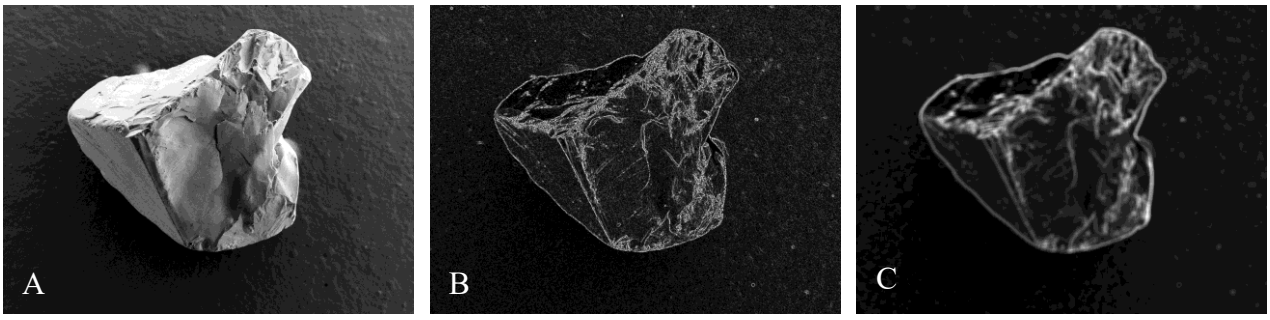


Figure 3.12. Images of Grain 3: A. SEM image. B. Edge map. C. Filtered edge density map.

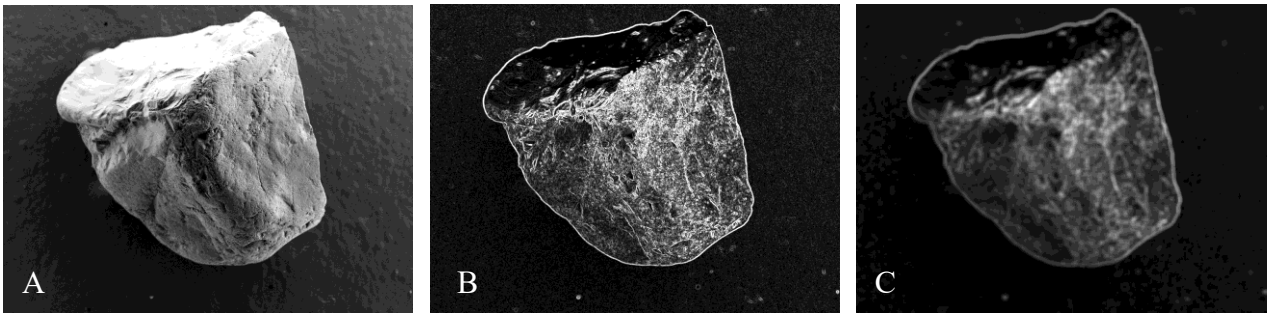


Figure 3.13. Images of Grain 4: A. SEM image. B. Edge map. C. Filtered edge density map.

While the reason for the different wicking velocities between grains is unknown, some clues can be found in higher resolution SEM images of surface structure. In the case of Grain 1, further examination showed that the surface exhibited significant micro porosity. Figure 3.14 shows high magnification images of Grain 1 while Figure 3.15 shows high magnification images of Grain 2. Comparing the two sets of high magnification SEM images, Grain 1 is full of holes while Grain 2 has a much smoother undulating surface with few isolated holes. This difference is

likely responsible the nearly 2 orders of magnitude difference observed in their measured wicking velocities. It is suspected that the water was being wicked into micro cracks and micropores existing within the grains and that surface spreading occurred because of this wicking and not as an independent process of its own. This discovery might explain why little to no flow was observed on some grains which had relatively rough surfaces.

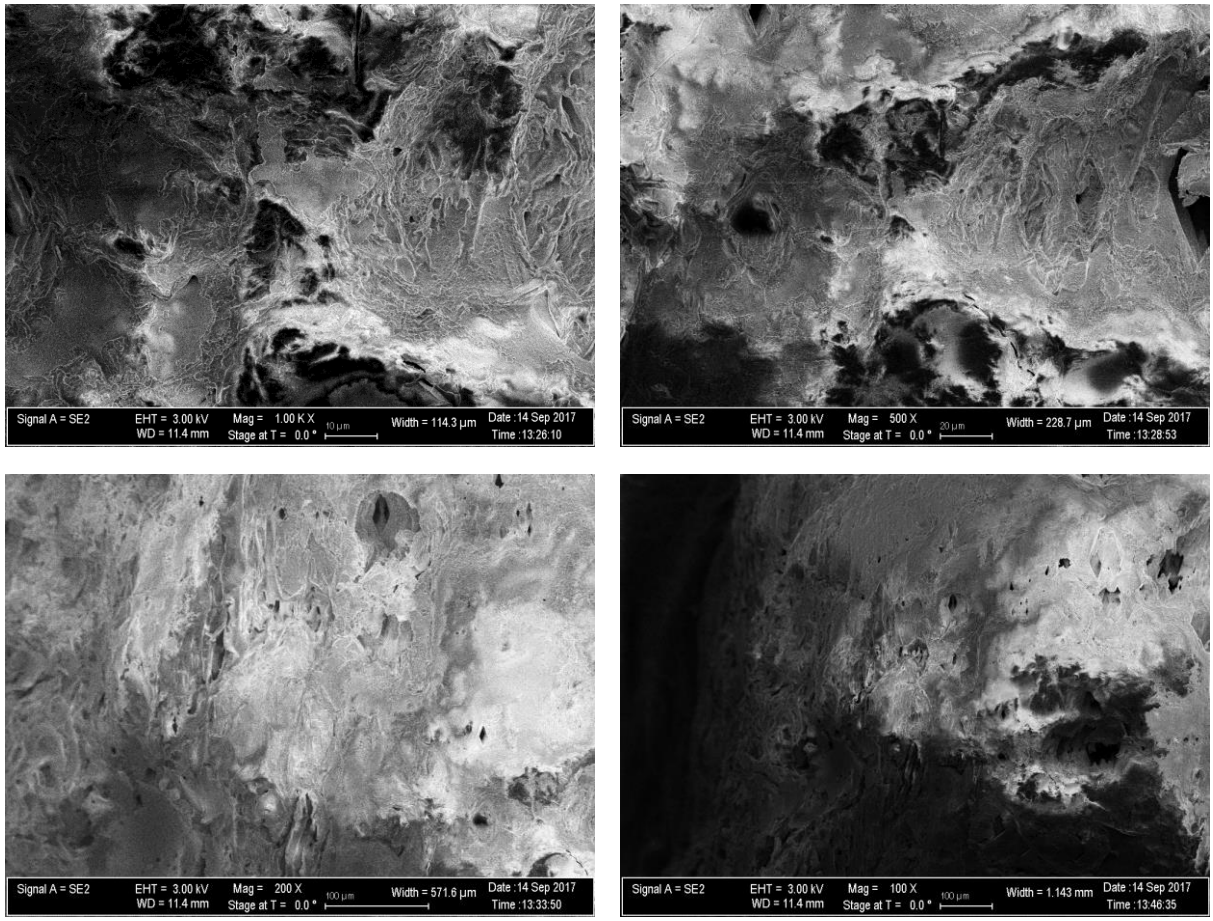


Figure 3.14. High magnification SEM images of Grain 1 showing surface roughness in form of micro-porosity. Surface contains holes of varying sizes as well as some undulations.

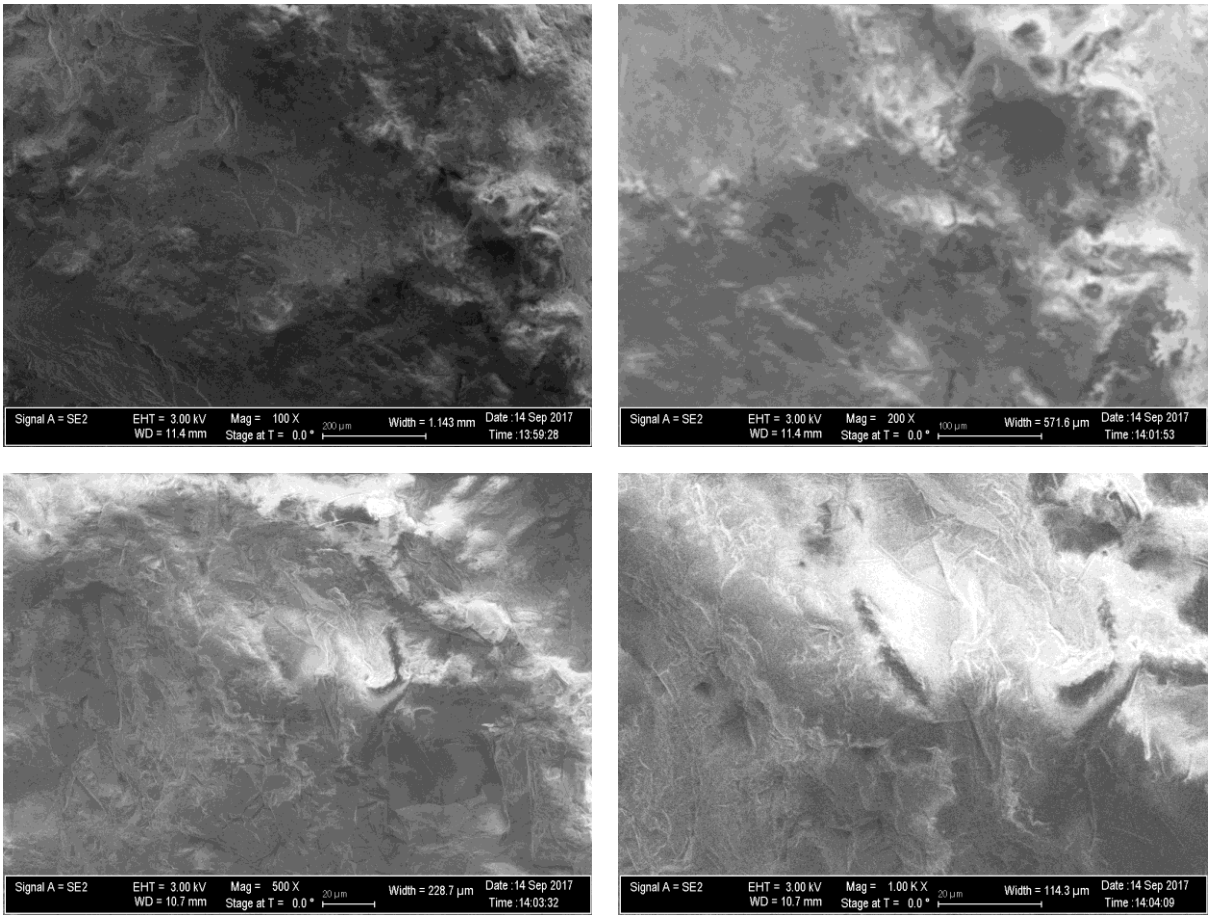


Figure 3.15. High magnification SEM images of Grain 2 showing surface roughness in form of undulation with some isolated holes.

For comparison, Figure 3.16 shows images of water spreading over concrete in 3 second intervals. Note that concrete is a highly-porous solid, so might be expected to exhibit wicking through a mechanism similar to Grain 1, although this situation is somewhat different from the experiments carried out on the sand grains because the water is initially under positive pressure and spreads out from the pool of water into the dry concrete. The observed wicking velocity on the concrete was even faster than the initial wicking velocity observed on Grain 1, suggesting that wicking on porous surfaces may be more rapid than nonporous surfaces.

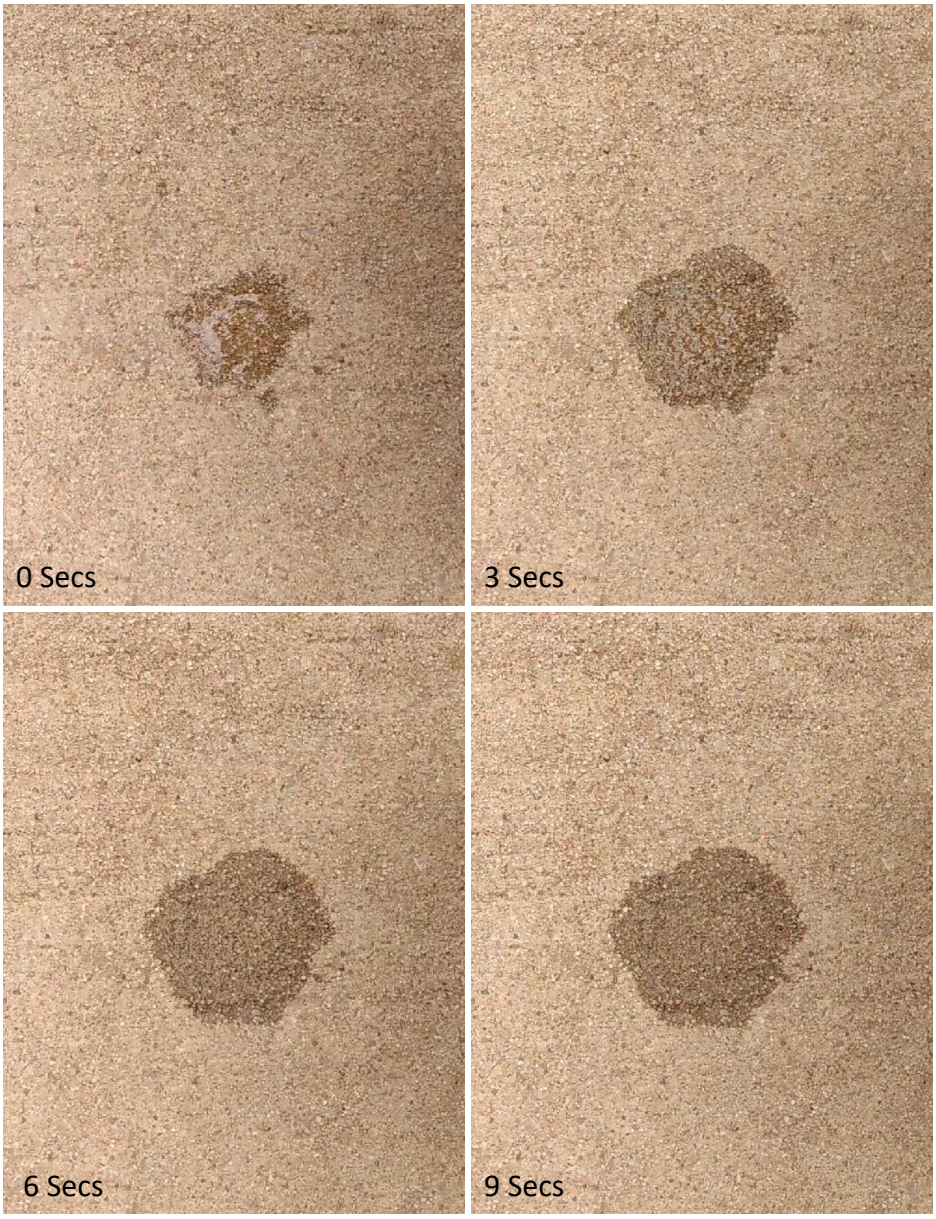


Figure 3.16. Images showing water spreading over concrete surface in 3 second intervals.

Table 3.1 shows the measured initial velocities for the surfaces studied in this chapter, illustrating the significantly higher velocities for porous surfaces (Grain 1, Concrete) compared with the less porous surfaces.

Experimental Surface	Observed average initial wetting front/wicking velocity (m/s)
Concrete	6.4×10^{-4}
Grain 1 (Inlet position 1)	9.25×10^{-5}
Grain 2	1.36×10^{-6}
Grain 3	0
Grain 4	0

Table 3.1. Table showing the initial wetting front/wicking velocities observed on experimental grains and concrete.

Figure 3.17 explores the Washburn Law for wicking on Grains 1 and 2. A plot of distance versus square root of time was made for Grain 1 and Grain 2 to compare the observed wicking on the grains to the Washburn Law which has been shown to hold true for rough surfaces (Cheng *et al.*, 2015). Figure 3.17A shows the plot for Grain 1 and Figure 3.17B shows the plot for Grain 2. The length in the plots refers to distance covered by the wetting front from source, and was calculated by taking the square root of the dye covered area on the grain surface for any point in time. The dye covered area was measured using the Fiji software (Schindelin *et al.*, 2012). The data points for Grain 1 had a much better linear correlation when compared to the data points for Grain 2. This is likely due to the micro-porosity of the surface of Grain 1 which is

absent in Grain 2. Because of the non-uniformity of the natural grain surfaces, it is expected that wicking velocity will vary as the liquid encounters different areas of roughness. For this reason, it is not surprising that Grain 1 did not exhibit a perfect linear correlation between wetting front distance and square root of time.

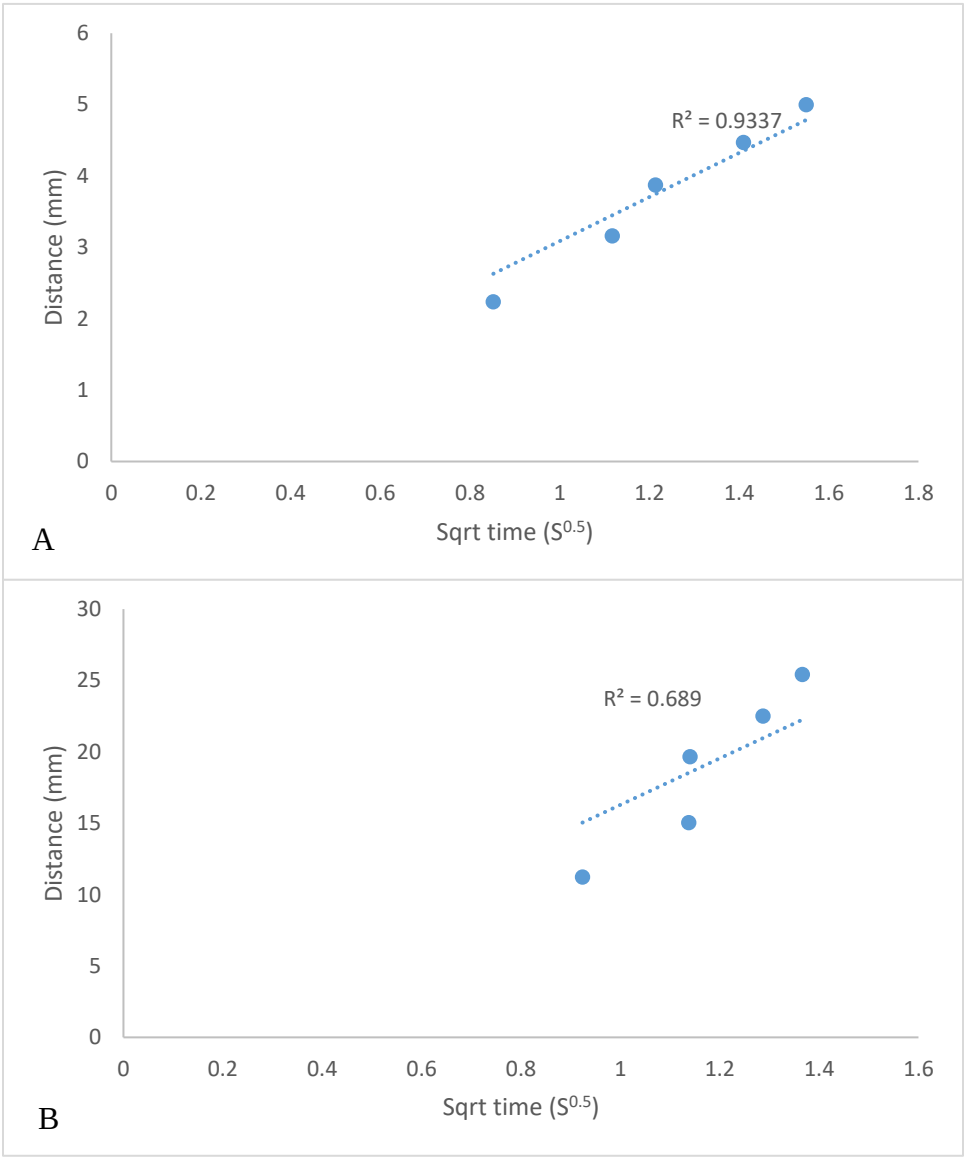


Figure 3.17. Images showing plots of distance versus square root of time for: A. Grain 1 and B. Grain 2.

3.4 Conclusions

The results of this work show that wicking occurs on grains that appear rough, but significant variability in initial wicking rate is observed. This is likely due to major differences in surface structure. Grains with surface micro-porosity exhibit rapid wicking.

As expected, smooth grains don't appear to exhibit any wicking. Some rough grains also don't exhibit any wicking. This again is likely due to differences in surface structure. Roughness in the form of smooth undulations alone is not likely to cause wicking.

On an individual rough grain, the pattern of wicking tends to follow roughness as indicated by edge detection. The Initial wicking velocities seem to correlate with the roughness of different points on a particular grain. Edge detection however is not a good predictor of velocity between different grains.

Chapter 4

Exploring the Impact of Long-Term Evaporation on the Relationship Between Capillary Pressure and Water Saturation in Unsaturated Porous Media

Abstract

The focus of this work was on understanding the impact of evaporation on the capillary pressure-saturation (P_c-S) state of a porous medium. Evaporation is ubiquitous near the ground surface in the vadose zone, but little is known about how evaporation impacts the relationship between capillary pressure and saturation. The hypothesis driving the work was that the P_c-S relationship is the result of an equilibrium between evaporative water loss, capillary forces, and the upward flow of water to replenish evaporated water. Experiments were conducted using two different porous media, a coarse sand and a nylon membrane with a 20 μm pore size. Long term evaporation experiments were conducted using different configurations to control evaporation within the media. Results found that increased accessibility to evaporation caused saturation in drainage P_c-S curves to decrease over time, causing the curves to become closer to imbibition P_c-S curves. In the membrane, the high external surface area to pore volume ratio introduced changes in evaporative flux to produce rapid changes in the P_c-S state of the medium. One implication of the work is that results suggest that long-term drainage experiments in vented columns may not necessarily provide a meaningful measurement of static P_c-S curve, but rather may be impacted by evaporation.

4.1. Introduction

The relationship between capillary pressure and water saturation in a porous medium is essential to understanding the behavior of the medium in its partially saturated state. Capillary pressure (P_c) is a measure of the difference in pressure between two immiscible (non-mixing) fluids in a porous medium. For unsaturated flow, the fluids are air and water. Below the water table in a natural porous medium (e.g., an aquifer), water is under positive pressure, while above the water table, water is under negative pressure. Positive capillary pressure is equivalent to negative water pressure, and is often measured in height units. In the absence of flow, capillary pressure is equivalent to the height above the water table. Saturation (S) is the ratio of the volume of water contained in the voids within a porous medium to the total volume of voids in the porous medium. Below the water table, a porous medium is fully saturated, meaning that only water fills the pores. Above the water table, a porous medium is unsaturated, meaning that both air and water are present in the pores. The relationship between capillary pressure and saturation is hysteretic, in that the capillary pressure observed at a given saturation depends on the wetting-drying history of the medium. In general, when water is drained out of a porous medium, a higher capillary pressure is observed at a given saturation compared with the case where water is allowed to imbibe (flow in) to the porous medium (Chen *et al.*, 2007).

The capillary pressure-saturation (P_c-S) relationship is an important input for a range of practical applications, including understanding and simulating contaminant fate and transport in multiphase systems (Pasha *et al.*, 2014; Hossain & Mumford, 2017), simulating slope stability (Chiu *et al.*, 2012; Rianna *et al.*, 2018), modeling pavement subsurface drainage (Lebeau & Konrad, 2009) and understanding the hydraulic performance of geosynthetic clay liners (Beddoe *et al.*, 2011). Many properties of porous media depend on the P_c-S relationship, including water

storage (Vaunat *et al.*, 2000; Huang *et al.*, 2011), shear strength (Fredlund *et al.*, 1996; Öberg & Sällfors, 1997; Vanapalli & Fredlund, 2000), hydraulic conductivity (Rawls *et al.*, 1998; Parent *et al.*, 2007), as well as structural properties such as tensile strength (Yin & Vanapalli, 2018) and resilient modulus for pavement design (Han *et al.*, 2016).

To develop accurate models capable of replicating experimental observations, it is important to understand the factors influencing the P_c-S relationship and the effects these factors have on the capillary pressure-saturation relationship. While the effects of many factors, such as fluid and porous medium properties, are well understood, little work has been reported examining the effect of evaporation on the P_c-S relationship. Because evaporation is a continuous occurrence near the ground surface in nature, this is a critical knowledge gap.

The hypothesis driving this work was that the P_c-S relationship is the result of an equilibrium between evaporative water loss, capillary forces, and the upward flow of water to replenish evaporated water. For a given system, increasing evaporation rate should lead to a lower P_c for a given S.

To explore this hypothesis, long-term evaporation experiments were conducted in a sand in two configurations with different capacities for evaporation, one a closed column where air could only enter the top, the other an open column vented along its entire length. Additional experiments were conducted using a membrane as the porous medium, to explore a system with a very high surface area to volume ratio, where evaporation was likely to dominate observed behavior.

4.2. Materials and Methods

4.2.1. Materials

Two porous media were used in experiments discussed in this paper, a sand and a membrane. The sand was US Silica (Ottawa, IL) F30 Sand, a coarse, high purity, foundry-grade sand with an average grain size (d_{50}) of 590 µm. The sand was used for long term evaporation experiments. The membrane was a supported nylon membrane with a 20 µm pore size purchased from GE Osmonics (Minnetonka, MN). The membrane was purchased in 293 mm diameter discs and cut into strips for the work as described below.

4.2.2. Experimental Procedures

Figure 4.1 shows the experimental configuration used for the sand. Two parallel columns of sand were packed into a frame made from 3.175 mm thick acrylic. The sand columns were 304.8 mm long, 25.4mm wide and 12.7mm thick. The closed column was covered on both the front and back face with acrylic, while the open column had acrylic was covered with acrylic on the front face, and a stainless steel #40 mesh screen on the back face to increase accessibility of air to the sand column. The bottoms of both columns were covered with the #40 mesh to hold the sand in place, while allowing water to imbibe or drain. The tops of both columns was left open to allow air to move freely in and out of the sand.

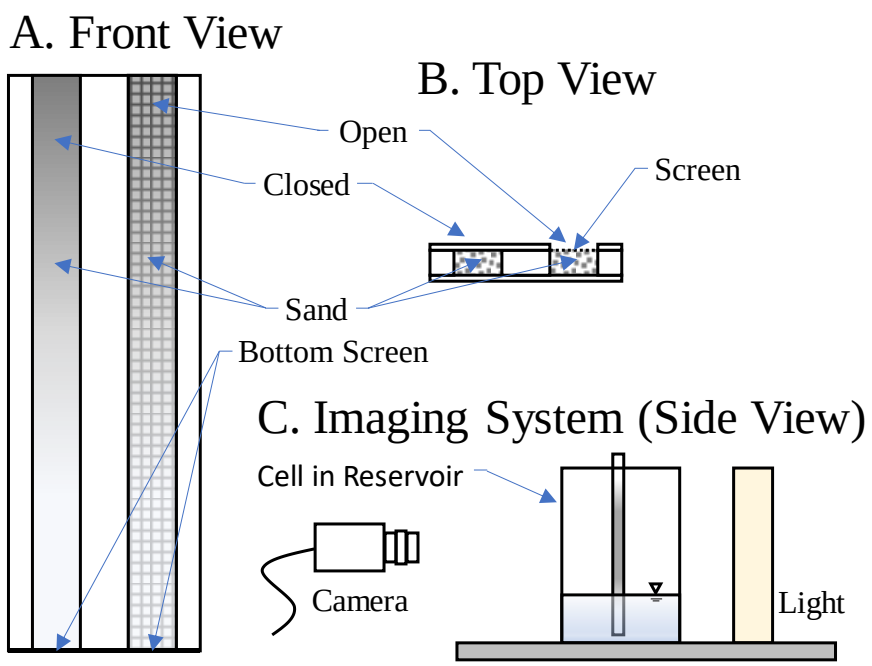


Figure 4.1. Schematic of the experimental system used for F30 Sand. A. Front view of the optical cell. B. Top view of the optical cell. C. Side view of the entire imaging system.

The samples were placed vertically in a clear plastic reservoir of length 193 mm, width 90 mm and height 280 mm. The reservoir had a small opening on the side near the bottom which was connected to a tank of identical dimensions with a clear plastic hose. The tank was filled with water and raised to fill the reservoir or lowered to drain it. The hose contained a valve along its length which could be open to allow flow between the reservoir and tank or closed to prevent flow between them.

Imaging for the experiment was done with a Basler puA1280-54uc camera and a Fujinon-TV zoom lens model H6x12.5R with a focal length range of 12.5 mm – 75 mm and maximum aperture f/1.2. Columns were backlit with a fluorescent backlight measuring 600 mm by 500

mm, consisting of two fluorescent tubes behind a translucent white plastic diffuser. Non-reflective opaque material was used to seal around the perimeter of the sample to ensure that only light from the samples reached the camera. There was a distance of 3.2 m between the experimental setup and the camera.

The reservoir was filled to a desired height by raising the tank above the reservoir, thus allowing water from the external tank to flow into the reservoir under gravity. Once the desired level water was reached in the reservoir, the valve on the hose was closed to stop the flow of water. The columns were allowed to imbibe with their bottom ends submerged in water for at least 24 hours or until the wetting front in the porous medium stabilized (stopped advancing). Next, the columns were completely saturated by opening the valve and letting water fill up the reservoir completely, submerging the columns. The columns were allowed to stand in the water for at least 12 hours, until no further change was observed in the columns. The water level was then lowered in the reservoir by lowering the tank level below the reservoir, opening up the valve and allowing water to flow out of the reservoir into the tank under gravity until the water level was again near the bottom of the columns. The columns were allowed to stand undisturbed. To prevent the water level from dropping too fast because of evaporation, a thin layer of flexible polymer foam was used to cover the exposed water surface in the reservoir. In addition, 30 to 50 mL of water was added directly to the reservoir daily. This allowed for a gradual drop of the water level over the course of the experiment, ensuring that drainage curves were observed. The columns were monitored by taking images of them at regular intervals. The long term drainage/evaporation experiment was continued until the water level in the reservoir dropped too low for its location to be observed in images.

A similar system was used to image the membrane. A rectangular piece of nylon membrane 290mm tall by 55mm wide was attached to a rectangular frame 310 mm tall and 76 mm wide. The frame was placed inside a clear reservoir identical to the one used for the sand columns. The procedures with the membrane were similar to those used with the sand columns, except the flexible polymer foam and regular water additions were not needed to slow the evaporation in the reservoir, because of the much shorter timescales of the experiments. Additional experiments were conducted to evaluate the effect of reducing evaporation by covering the reservoir containing the membrane with polyethylene cling wrap.

Images were processed using a Python program written for the work. The program calculates saturation as a function of height using the light transmission approach used previously by Naghavi and Kibbey (2014) , with the exception that an image of a fully dry medium was used in place of a medium at residual saturation so that saturation could be calculated directly. For this work, intensity was averaged at each elevation to yield a single saturation value for each elevation. Note that because of differences in the refraction by wet vs. dry porous media, images of saturated media are brighter than images of dry media.

4.3. Results and Discussion

Figure 4.2 shows selected images from a long-term experiment conducted with the F30 sand. Image pairs are shown for the closed (left) and open (right) system at different wetting or drying states. Note that the water levels in the reservoir have been aligned in the images to allow direct comparison between images. The leftmost image pair shows the columns after spontaneous imbibition into initially-dry columns had stabilized and was no longer changing; the

image shown corresponds to 39 hours after the start of imbibition. (Note that a subsequent experiment in a different packing of the same media found no measurable change in water content above the air entry pressure for the open or closed systems over two weeks after imbibition had initially stabilized, so the curve in the figure can be considered representative of equilibrium imbibition.)

The remaining five image pairs in Fig. 4.2 show drainage over the course of 60 days. The image labeled t=0 is the image that was taken immediately after the water level was initially dropped to begin the process of draining the columns from their fully saturated state. It is apparent from the images that substantial drainage had occurred within the first hour within both the open and closed systems. Over the remainder of the 60 days, both the open and closed systems continued to change at much slower rates, with the saturated (bright) portion of each column gradually decreasing in height in each case. While some of the initial decrease in both systems (e.g., over the first day in the images, perhaps slightly) likely includes contributions from continued drainage, it is likely that the longer term changes in both systems result from evaporation.

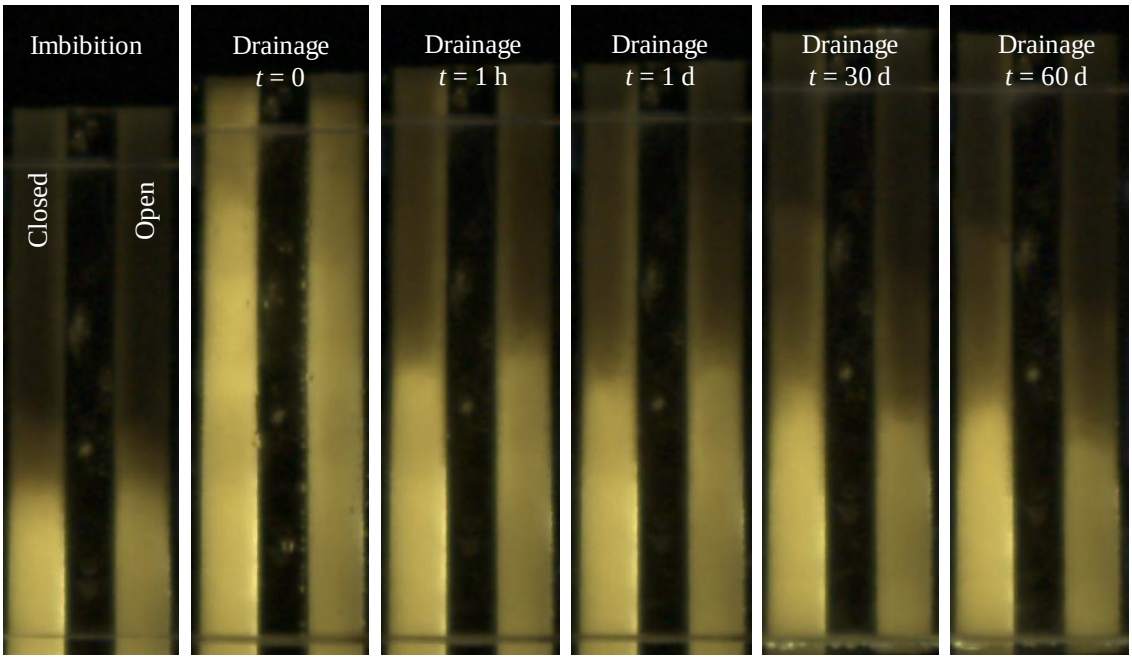


Figure 4.2. Images of F30 sand showing imbibition, and then drainage/evaporation over 60 days. The closed system is on the left, and the open system is on the right. Brighter pixels correspond to higher saturation. Note that images have been shifted vertically to align water levels, which were allowed to drop gradually during drainage.

Figure 4.3 shows P_c-S drainage curves calculated from the images for the F30 sand systems over a period of 117.7 days. Imbibition curves are also shown for reference. Note that the noise at low saturations in Figure 4.3 is the result of the image noise and the log form of the equation used to calculate saturation (Naghavi & Kibbey, 2014). Figure 4.3A corresponds to the closed system, while Figure 4.3B corresponds to the open system. Figure 4.3A shows initial rapid drainage which occurred within the first 2 hours of draining the samples, after which little change is evident over much of the P_c-S curve. (It should be noted that elevation and capillary pressure are not equivalent in cases where there is significant pressure-driven vertical flow, so the curves from the first few hours of drainage are not P_c-S curves, but rather are plots of

elevation vs. *S*.) Only the top portion of the closed column – the portion initially near residual saturation, above the capillary fringe – continued to decrease in

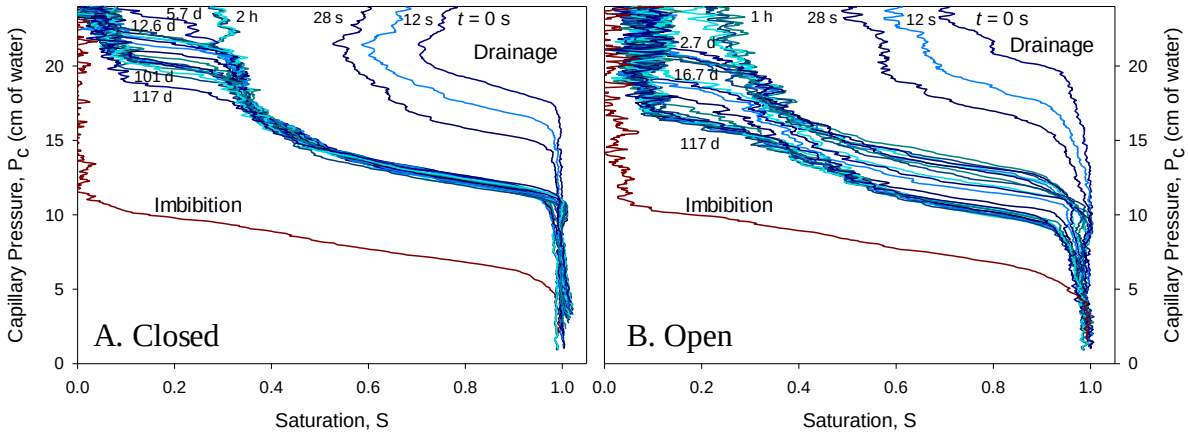


Figure 4.3. P_c-S curves for the F30 sand showing spontaneous imbibition curves (in red), and drainage curves corresponding to evaporation over 117 days (in blue). Curves shown correspond to A. the closed system, and B. the open system. Times of selected curves are labeled.

saturation over the remainder of the 117.7 days. After 5.7 days, the saturation at the very top of the closed sample had dropped to approximately zero. Over the next 111 days, the saturation of the top 6 cm of the closed sample continued to gradually decrease, as a drying front moved down the column from the open top. In contrast, no change is observed lower in the column. (Note that the curves between 12.6 and 101 days are plotted at 7-day intervals.) Because the experiment ended when the water became too low in the reservoir to observe the water level (the datum from which capillary pressure is measured), it is not known whether the drying front would have ultimately continued down into the capillary fringe. However, the higher wetting phase relative permeability in more saturated capillary fringe compared with the portion higher in the column initially near residual saturation likely means that upward flow of water through

the capillary fringe would be greater than higher in the column, so could potentially provide water at a greater rate. It is probable there is an equilibrium P_c-S curve, perhaps not too different from the 117.7 day curve, where water flow balances evaporation, and no further change is observed over time. This is made increasingly likely by the larger zone of dry sand at the top of the column, a situation which has been reported by others to slow evaporation (e.g., (Good *et al.*, 2015; Balugani *et al.*, 2018)).

Like the closed system (Fig. 4.3A), the open system (Fig. 4.3B) shows both rapid initial drainage, and gradual evaporation above the capillary fringe. Unlike the closed system, however, the open system exhibits two major differences. First, the initial drainage in the capillary fringe (the higher saturation portion) was actually slower for the open system than the closed system. Note that at 1 h, the capillary pressures were actually higher in the open system (Fig. 4.3B) than in the closed system at high saturations. This is likely because air entering lower in the column slows drainage of water from the top of the column by reducing the wetting phase relative permeability lower in the column; a similar phenomenon has been identified as the source of boundary induced saturation inversion in rapidly-draining columns (e.g.,(Kibbey *et al.*, 2016)). Second, unlike the closed system (Fig. 4.3A), the higher saturation region of the open column (Fig. 4.3B) continued to gradually decrease in saturation to well beyond the time when the high saturation region of the closed system had stopped changing. Only after approx. 60 days did the capillary fringe of the open system appear to stop changing. While the capillary pressures in the open system (Fig. 4.3B) appear to have plateaued at levels higher than the imbibition curve, they are lower than in the closed system (Fig. 4.3A). The difference in response to evaporation between the two systems likely results from the different air accessibility between them producing different evaporation rates. The greater area for air mass transfer in the

open system produces a higher rate of evaporative water removal from the column than in the closed system, yielding a different equilibrium between upward water flow and evaporation.

Figure 4.4 provides a direct comparison between the imbibition and long term drainage P_c-S curves for both the closed and open systems in Fig. 4.3. It is apparent from the figure that the long-term drainage curve in the open system is significantly lower than in the closed system. Note that the two imbibition curves are virtually identical, a fact that highlights that the observed differences in behavior could not have resulted from differences in packing between the two systems.

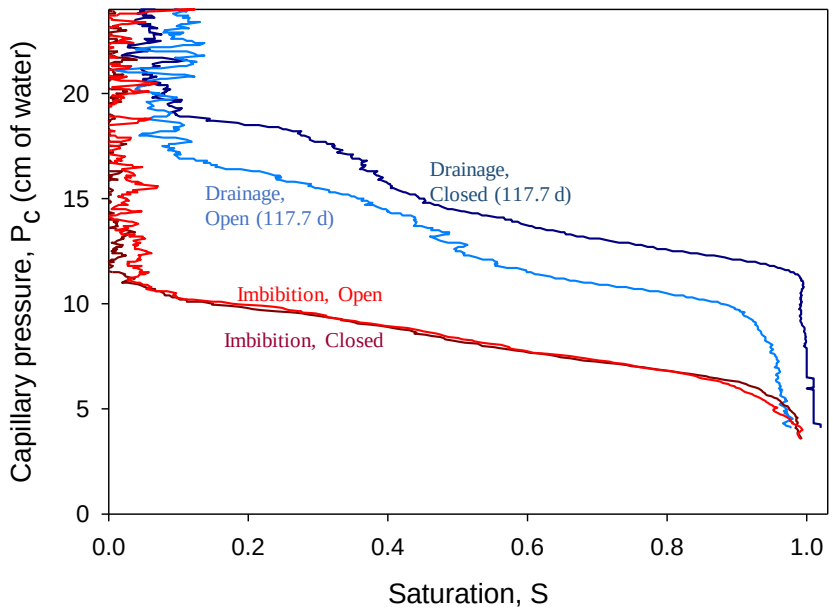


Figure 4.4. Comparison between P_c-S curves in the open and closed systems for F30 sand, showing spontaneous imbibition, and drainage curves after 117.7 days of evaporation.

Figures 4.5 and 4.6 further illustrate the differences between the closed and open systems. Figure 4.5 shows the elevation from the water table as a function of time for water saturations of 0.2, 0.4, 0.6 and 0.8 in the F30 sand systems. Fig. 4.5A corresponds to the closed system, while Fig. 4.5B corresponds to the open system. Note that elevations in the closed system (Fig. 4.5A) stabilize rapidly for all but the lowest saturation (0.2), exhibiting virtually no change over the duration of the experiment. In contrast, elevations at all saturations in the open system continue to decrease over time up to approx. 60 days. After 60 days, elevations at the lowest saturation (0.2) continue to decrease. Figure 4.6 shows ratios of the curves in Fig. 4.5A and B, illustrating both the lower initial elevation in the closed system (likely due to the slowed initial drainage in the open system), and then the extent to which evaporation causes the behavior of the two to deviate for approx. 60 days, after which steady state configurations are reached (i.e., the long-term drainage curves in Fig. 4.4).

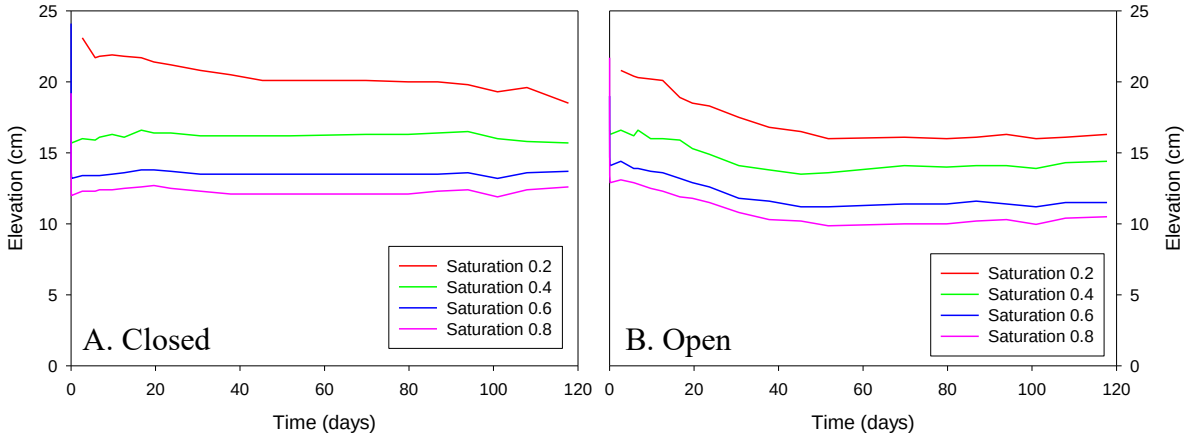


Figure 4.5. Elevation vs. time at four saturation levels in the F30 sand for the A. closed and B. open systems.

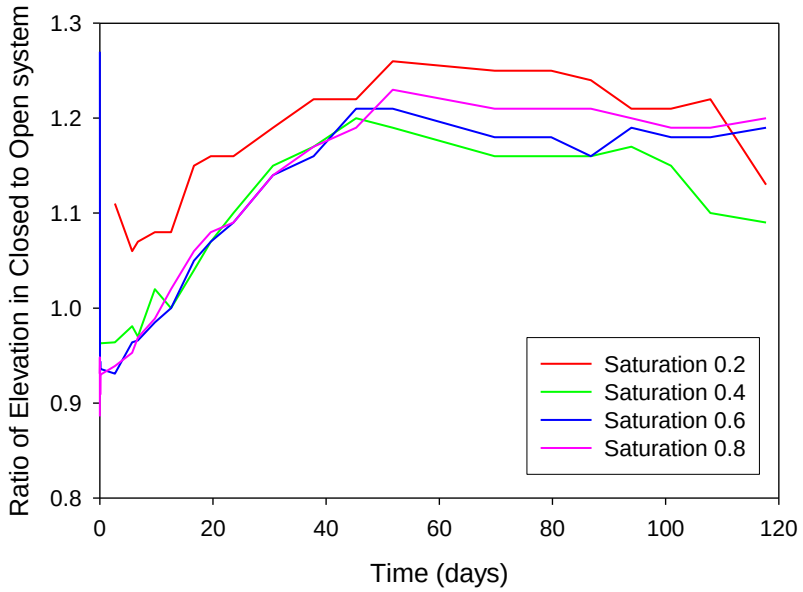


Figure 4.6. Ratio of elevation in open and closed systems vs. time at four saturation levels in the F30 sand.

To better understand the differences in behavior between the open and closed sand systems, experiments were conducted using a porous nylon membrane as the porous medium. The membrane is like an extreme case of the open system, with a very high external surface area to volume ratio. That fact should accentuate the effect of evaporation on water configuration in the system.

Figure 4.7 shows selected images from a drainage experiment with the membrane. The leftmost image shows the membrane after spontaneous imbibition from an initially dry state. The remaining images show drainage after 0, 24 and 48 hours. Note that the water levels in the reservoir have been aligned in the images to allow direct comparison between images.

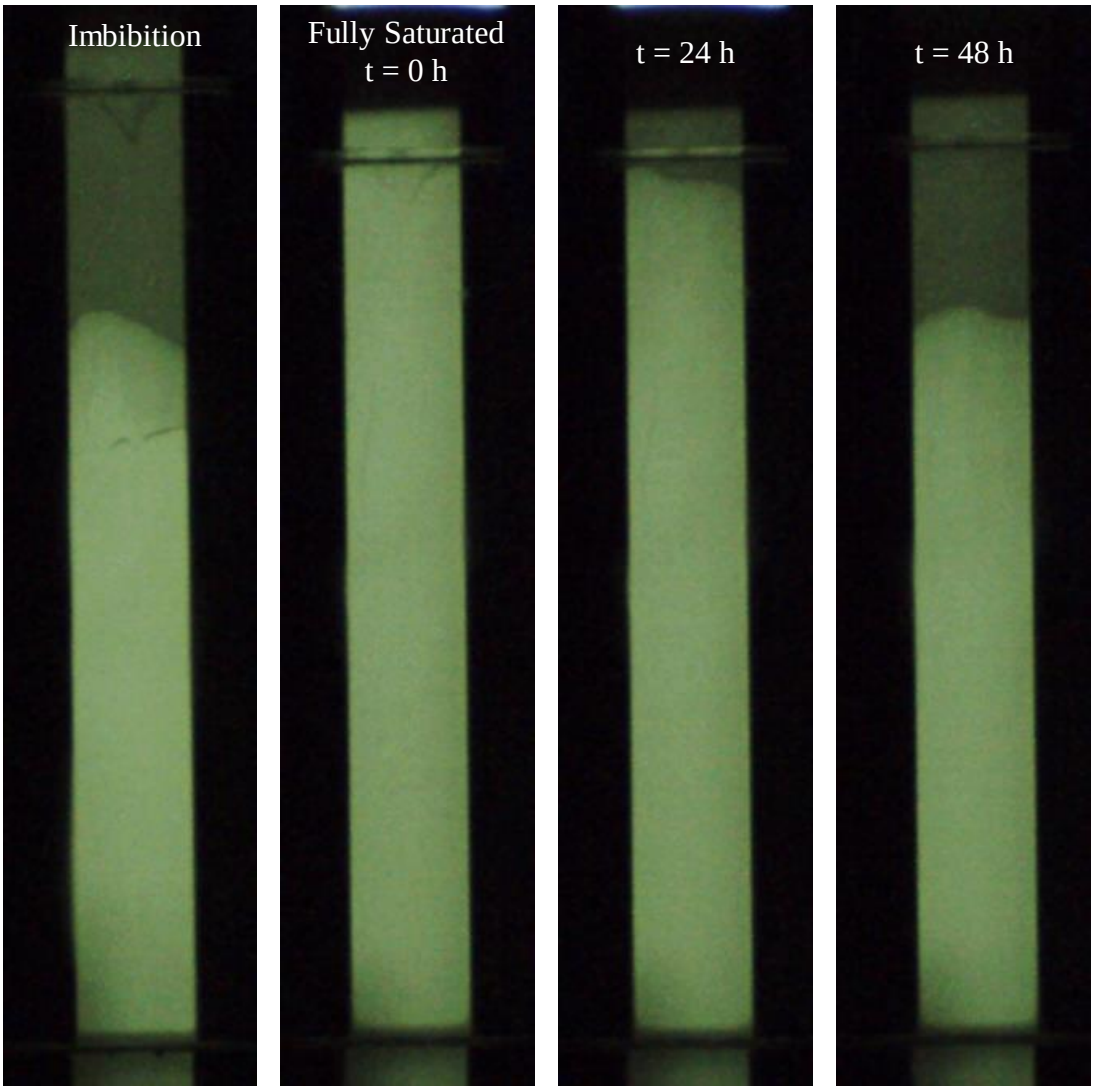


Figure 4.7. Images of the membrane showing imbibition, and then drainage/evaporation over 48 h.

Figure 4.8 shows P_c-S drainage curves calculated from the images for the membrane over a period of 63 h. The imbibition curve is also shown for reference. Note that the evaporation in the system occurs much more rapidly than in the sand systems, so after approx. 48 hours, the drainage curves had evaporated to the imbibition curve, after which no change was observed.

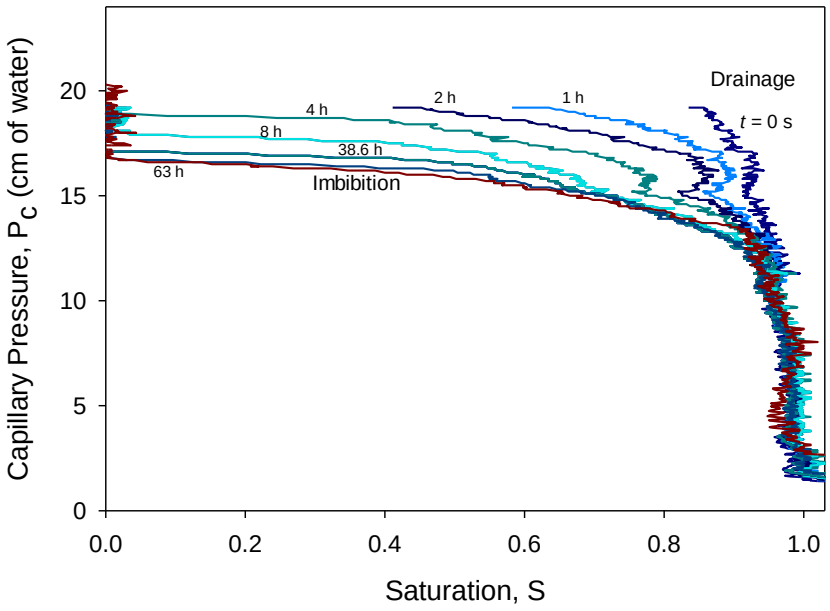


Figure 4.8. Imbibition and drainage (evaporation) for the membrane. Note that subsequent experiments found that the true drainage curve is above the top of the membrane; evaporation causes saturation to decrease until the curve matches the imbibition P_c-S curve.

Subsequent experiments with the reservoir covered with polyethylene cling wrap were conducted as a means of slowing evaporation from the membrane by increasing humidity in the air around it. The experiments led to the interesting discovery that both the imbibition and drainage curves were above the top of the membrane in the covered system. That is, if the reservoir were covered, an initially saturated membrane would never drain (the air entry pressure

was above the top of the membrane). And if an imbibition experiment were conducted in the covered reservoir, the water would rapidly rise to the top of the membrane.

This phenomenon is illustrated in Figure 4.9, which shows the elevation above the water table where S = 0.4 for another membrane experiment. Note that elevation decreases over the course of approx. 5 d as evaporation occurs, after which the elevation remains approximately steady. (The plateau is slightly lower than in Fig. 8, presumably because of slightly different ambient temperature or humidity at the times the experiments were conducted.) Just after 8 days, the reservoir containing the membrane was covered, increasing the moisture content in the air around the membrane by preventing equilibration between water and the reservoir and the surrounding room.

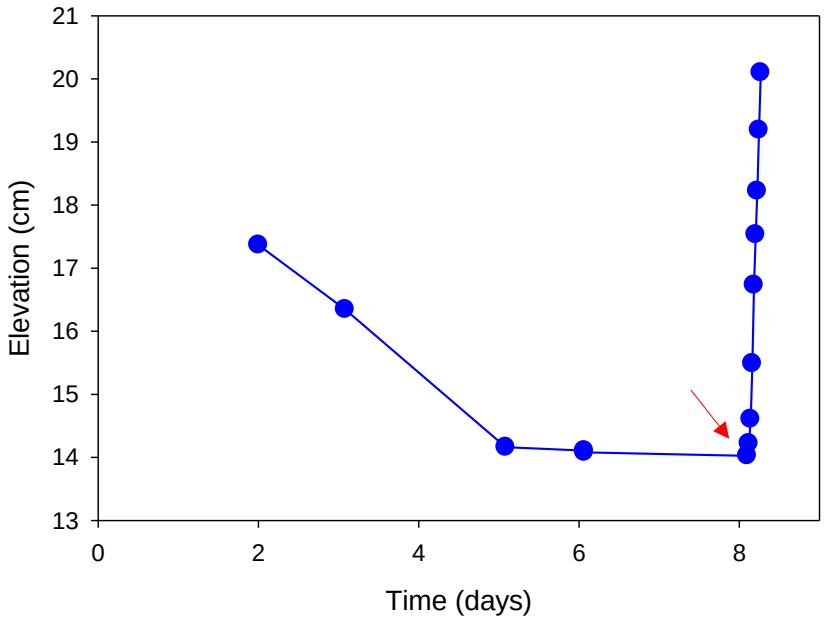


Figure 4.9. Drainage/evaporation of a membrane followed by rapid imbibition induced by covering the reservoir to slow evaporation. The plot shows the elevation of the portion of the membrane where S=0.4 as a function of time. The arrow indicates the time the reservoir was covered.

It is apparent from the figure that the membrane rapidly re-saturates once the reservoir is covered, highlighting the link between evaporation rate and the P_c-S state. Covering the reservoir decreases the driving force for evaporation, slowing its rate, and ultimately yielding a different equilibrium relationship between P_c and S throughout the membrane.

4.4. Conclusions

Results of this work suggest that there is a link between the observed P_c-S relationship in a porous medium, and the rate of evaporation. Systems where evaporation is significant exhibit long term changes in the P_c-S state, with drainage P_c-S curves appearing to gradually drop towards imbibition curves over time. (No changes were observed in evaporating imbibition curves under constant evaporation conditions.) In a closed column where evaporation could occur at from the top of the column, saturation decreased only at the top of the column, where moisture content was near residual saturation. This was likely both due to the fact that evaporation only occurred from the open top of the column, and the fact that relative permeability is low at low saturation, slowing upward flow to replenish the evaporated porewater. In an open column, where evaporation could occur along the length of the column, saturation gradually decreased over the entire height of the profile. Experiments conducted with a membrane as the porous medium found that the high external area to volume ratio caused evaporation rate to play a substantial role in the P_c-S behavior. Drainage curves were observed to evaporate down to match imbibition curves. Furthermore, changing the evaporation rate by closing an open system led to rapid changes in P_c-S state for the membrane.

A practical implication of the results of this work is that long term experiments in a column vented along its length may not necessarily be representative of equilibrium capillary pressure measurements, but may reflect the effects of evaporation. There are many historical examples in the literature where vented columns are used to measure static capillary pressures for comparison with dynamic measurements (e.g., (Rogers & Klute, 1971)); depending on the extent of venting, those measurements may not be true static values, so may not really be appropriate for comparison with dynamic measurements. The work also suggests that equilibrium P_c-S state in some systems may depend not only on capillary forces, but also on conditions that influence evaporation.

Chapter 5

Summary and Conclusions

5.1 Conclusions

Fluid motion in unsaturated porous media and the transport that occurs with it are of great interest across several disciplines. This study examined a range of important processes which occur in unsaturated porous media from the grain scale to the continuum scale.

The work in Chapter 2 explored the effect of evaporation on soluble contaminant deposition on rough surfaces. Natural sand grains were covered with solutions of sodium chloride and sucrose and allowed to dry through evaporation. The patterns of precipitates formed on surfaces were studied using SEM imaging and EDS. Results suggest that as evaporation progresses, the water films recede towards the grain surface but remain pinned on the high points. As the concentration of solution increases due to evaporation, there is an outward advection of the solute towards areas of lower concentration, in this case, towards to edges of the liquid films which have been pinned on high points of the grain surface. Results also suggest that this outward flow might be hindered if the viscosity of the concentrated solution becomes too high to allow easy outward flow. A practical implication of the work is that there might be an initially high mass transfer of solute during subsequent dissolution because of the large precipitate surface area from low-thickness precipitates, which should decrease early in the dissolution process as low-thickness precipitates are dissolved from the surface, leaving only localized thicker precipitates

The work in Chapter 3 explored the effects of surface roughness on the wicking patterns of capillary films onto initially dry surfaces. SEM imaging and edge detection were used to

generate edge density maps for the grain surfaces as an indication of the roughness of the grain. Brighter edge maps indicated a rougher grain surface. Water dyed with Sulforhodamine B was used to enhance the visibility of water films. The wicking patterns were monitored by taking regular images of the grain over time. Results showed that water tends to flow on the rougher portions of the grain as indicated by the edge density maps. Results also showed that edge density maps alone were insufficient to determine whether wicking will on a grain or not. Roughness in the form of micro-porosity appears to be required for rapid wicking to occur.

The work in Chapter 4 studied the effects of long-term evaporation on the P_c-S curves of a porous medium. Two porous media were used in the study. They were saturated, drained and then exposed to evaporation for 117 days. Results show that systems where evaporation is significant exhibit long term changes in the P_c-S state, with drainage P_c-S curves appearing to gradually drop towards imbibition curves over time. Results also show that the external area to volume ratio of a porous medium plays a substantial role in the P_c-S behavior where a higher ratio causes a higher magnitude drop in drainage curve toward imbibition curve. A practical implication of the results of this work is that long term experiments in a column vented along its length may not reflect true static P_c and S values, so may not really be appropriate for comparison with dynamic measurements. Results also suggests that equilibrium P_c-S state in some systems may depend not only on capillary forces, but also on conditions that influence evaporation.

5.2 Recommendations for Future Work

Some suggestions for further work which could build on the findings of this work are discussed below.

For the work discussed in Chapters 2 and 3, manufactured surfaces with known roughness characteristics could be used to eliminate the variability that comes with using natural surfaces. One example of a type of material that could be used would be a structured abrasive. This approach could also potentially eliminate edge effects, and provide more insight into the mechanisms of flow for the grains with slow flow in Chapter 3. For Chapter 2, different solutes could be added to the study to further investigate viscosity effects in precipitate formation.

For the work described in Chapter 4, volatile liquids such as alcohol could be used instead of water in the study. The high volatility of the liquids would allow the evaporation experiments to proceed at a faster rate and come to equilibrium much quicker than the air-sand-water system, and could also provide another mechanism of controlling the relative importance of evaporation. Furthermore, the experiment could be designed to ensure that the liquid in the reservoir is maintained at a constant level so that there is no risk of stopping the experiment before it equilibrates. Finally, some modeling work could be done to provide more insight into the relationship between temperature, humidity and P_c-S curves.

References

Balugani, E., Lubczynski, M., van der Tol, C. & Metselaar, K. (2018) Testing three approaches to estimate soil evaporation through a dry soil layer in a semi-arid area. *Journal of hydrology*, **567**, 405-419.

Bear, J. (1972) Dynamics of fluids in porous media. *Hydrodynamic Dispersion*, 579-663.

Beddoe, R. A., Take, W. A. & Rowe, R. K. (2011) Water-retention behavior of geosynthetic clay liners. *Journal of Geotechnical and Geoenvironmental Engineering*, **137**, 1028-1038.

Bergstad, M. & Shokri, N. (2016) Evaporation of NaCl solution from porous media with mixed wettability. *Geophysical Research Letters*, **43**, 4426-4432.

Bico, J., Tordeux, C. & Quéré, D. (2001) Rough wetting. *EPL (Europhysics Letters)*, **55**, 214.

Borodin, S., Volkov, A. & Kazanskiĭ, N. (2009) Device for analyzing nanoroughness and contamination on a substrate from the dynamic state of a liquid drop deposited on its surface. *Journal of Optical Technology*, **76**, 408-412.

Butt, H.-J. & Kappl, M. (2009) Normal capillary forces. *Advances in colloid and interface science*, **146**, 48-60.

Cazabat, A. & Stuart, M. C. (1986) Dynamics of wetting: effects of surface roughness. *The Journal of Physical Chemistry*, **90**, 5845-5849.

Chen, L., Miller, G. A. & Kibbey, T. C. (2007) Rapid pseudo-static measurement of hysteretic capillary pressure-saturation relationships in unconsolidated porous media. *Geotechnical Testing Journal*, **30**, 474-483.

Chen, X. B., Nouri, A., Li, Y. C., Lin, J. G., Hodgson, P. D. & Wen, C. (2008) Effect of surface roughness of Ti, Zr, and TiZr on apatite precipitation from simulated body fluid. *Biotechnology and Bioengineering*, **101**, 378-387.

Chen, Y., Melvin, L. S., Rodriguez, S., Bell, D. & Weislogel, M. M. (2009) Capillary driven flow in micro scale surface structures. *Microelectronic Engineering*, **86**, 1317-1320.

Cheng, C.-L., Perfect, E., Donnelly, B., Bilheux, H. Z., Tremsin, A. S., McKay, L., *et al.* (2015) Rapid imbibition of water in fractures within unsaturated sedimentary rock. *Advances in water resources*, **77**, 82-89.

Chiu, C., Yan, W. & Yuen, K.-V. (2012) Reliability analysis of soil–water characteristics curve and its application to slope stability analysis. *Engineering Geology*, **135**, 83-91.

Darbha, G. K., Fischer, C., Luetzenkirchen, J. & Schafer, T. (2012) Site-Specific Retention of Colloids at Rough Rock Surfaces. *Environmental Science & Technology*, **46**, 9378-9387.

Fredlund, D. G., Xing, A., Fredlund, M. D. & Barbour, S. (1996) The relationship of the unsaturated soil shear to the soil-water characteristic curve. *Canadian Geotechnical Journal,* **33**, 440-448.

Good, S. P., Noone, D. & Bowen, G. (2015) Hydrologic connectivity constrains partitioning of global terrestrial water fluxes. *Science,* **349**, 175-177.

Gray, W. G. & Hassanizadeh, S. M. (1991) Unsaturated flow theory including interfacial phenomena. *Water Resources Research,* **27**, 1855-1863.

Han, Z., Vanapalli, S. K. & Zou, W.-l. (2016) Integrated approaches for predicting soil-water characteristic curve and resilient modulus of compacted fine-grained subgrade soils. *Canadian Geotechnical Journal,* **54**, 646-663.

Helliwell, J., Sturrock, C., Grayling, K., Tracy, S., Flavel, R., Young, I., *et al.* (2013) Applications of X-ray computed tomography for examining biophysical interactions and structural development in soil systems: a review. *European Journal of Soil Science,* **64**, 279-297.

Hendrickx, J. M. & Flury, M. (2001) Uniform and preferential flow mechanisms in the vadose zone. *Conceptual models of flow and transport in the fractured vadose zone*, 149-187.

Hird, R. & Bolton, M. D. (2017) Clarification of capillary rise in dry sand. *Engineering Geology,* **230**, 77-83.

Hossain, S. Z. & Mumford, K. G. (2017) Capillary pressure-saturation relationships for diluted bitumen and water in gravel. *Journal of hydrology*, **551**, 306-313.

Hou, X., Yin, G., Chen, X., Liao, X., Yao, Y. & Huang, Z. (2011) Effect of akermanite morphology on precipitation of bone-like apatite. *Applied Surface Science,* **257**, 3417-3422.

Hu, Q. & Wang, J. S. (2003) Aqueous-phase diffusion in unsaturated geologic media: a review.

Huang, M., Lee Barbour, S., Elshorbagy, A., Zettl, J. D. & Cheng Si, B. (2011) Infiltration and drainage processes in multi-layered coarse soils. *Canadian Journal of Soil Science,* **91**, 169-183.

Ishino, C., Reyssat, M., Reyssat, E., Okumura, K. & Quere, D. (2007) Wicking within forests of micropillars. *EPL (Europhysics Letters),* **79**, 56005.

Iwamatsu, M. (2017) Topography-and topology-driven spreading of non-Newtonian power-law liquids on a flat and a spherical substrate. *Physical Review E,* **96**, 042803.

Kamai, T., Weisbrod, N. & Dragila, M. I. (2009) Impact of ambient temperature on evaporation from surface-exposed fractures. *Water resources research,* **45**.

Kibbey, T. C. (2013) The configuration of water on rough natural surfaces: Implications for understanding air-water interfacial area, film thickness, and imaging resolution. *Water Resources Research,* **49**, 4765-4774.

Kibbey, T. C. & Chen, L. (2012) A pore network model study of the fluid-fluid interfacial areas measured by dynamic-interface tracer depletion and miscible displacement water phase advective tracer methods. *Water Resources Research,* **48**.

Kibbey, T. C., Naghavi, B. & Hou, L. (2016) Understanding the role of water phase continuity on the relationship between drainage rate and apparent residual saturation: A dynamic network model study. *Transport in Porous Media,* **112**, 689-705.

Kibsgaard, J., Chen, Z., Reinecke, B. N. & Jaramillo, T. F. (2012) Engineering the surface structure of MoS2 to preferentially expose active edge sites for electrocatalysis. *Nature materials,* **11**, 963-969.

Kim, B. S., Choi, G., Shim, D. I., Kim, K. M. & Cho, H. H. (2016) Surface roughening for hemi-wicking and its impact on convective boiling heat transfer. *International Journal of Heat and Mass Transfer,* **102**, 1100-1107.

Kim, B. S., Lee, H., Shin, S., Choi, G. & Cho, H. H. (2014) Interfacial wicking dynamics and its impact on critical heat flux of boiling heat transfer. *Applied Physics Letters,* **105**, 191601.

Kim, T. W., Tokunaga, T. K., Bargar, J. R., Latimer, M. J. & Webb, S. M. (2013) Brine film thicknesses on mica surfaces under geologic CO2 sequestration conditions and controlled capillary pressures. *Water Resources Research,* **49**, 5071-5076.

Kissa, E. (1996) Wetting and wicking. *Textile Research Journal,* **66**, 660-668.

Lai, C. Q., Mai, T. T., Zheng, H., Zheng, W., Lee, P., Leong, K., *et al.* (2014) Effects of structural and chemical anisotropy of nanostructures on droplet spreading on a two dimensional wicking surface. *Journal of Applied Physics,* **116**, 034907.

Lebeau, M. & Konrad, J.-M. (2009) Pavement subsurface drainage: importance of appropriate subbase materials. *Canadian Geotechnical Journal,* **46**, 987-1000.

Lebeau, M. & Konrad, J. M. (2010) A new capillary and thin film flow model for predicting the hydraulic conductivity of unsaturated porous media. *Water Resources Research,* **46**.

McHale, G., Shirtcliffe, N., Aqil, S., Perry, C. & Newton, M. (2004) Topography driven spreading. *Physical review letters,* **93**, 036102.

McKinley, J. P., Zachara, J. M., Liu, C., Heald, S. C., Prenitzer, B. I. & Kempshall, B. W. (2006) Microscale controls on the fate of contaminant uranium in the vadose zone, Hanford Site, Washington. *Geochimica et Cosmochimica Acta,* **70**, 1873-1887.

Meakin, P. & Tartakovsky, A. M. (2009) Modeling and simulation of pore-scale multiphase fluid flow and reactive transport in fractured and porous media. *Reviews of Geophysics,* **47**.

Mohammad, O. I. & Kibbey, T. C. G. (2005) Dissolution-induced contact angle modification in dense nonaqueous phase liquid/water systems. *Environmental Science & Technology,* **39**, 1698-1706.

Muthiah, P., Bhushan, B., Yun, K. & Kondo, H. (2013) Dual-layered-coated mechanically-durable superomniphobic surfaces with anti-smudge properties. *Journal of colloid and interface science,* **409**, 227-236.

Nachshon, U., Shahraeeni, E., Or, D., Dragila, M. & Weisbrod, N. (2011) Infrared thermography of evaporative fluxes and dynamics of salt deposition on heterogeneous porous surfaces. *Water Resources Research,* **47**.

Nachshon, U. & Weisbrod, N. (2015) Beyond the salt crust: on combined evaporation and subflorescent salt precipitation in porous media. *Transport in Porous Media,* **110**, 295-310.

Naghavi, B. & Kibbey, T. C. (2014) An experimental study of the factors influencing apparent wetting phase residual saturation in dynamically drained porous media. *Transport in porous media,* **101**, 149-160.

Öberg, A. & Sällfors, G. (1997) Determination of shear strength parameters of unsaturated silts and sands based on the water retention curve. *Geotechnical Testing Journal,* **20**, 40-48.

Oliver, J. & Mason, S. (1977) Microspreading studies on rough surfaces by scanning electron microscopy. *Journal of Colloid and Interface Science,* **60**, 480-487.

Oliver, J. & Mason, S. (1980) Liquid spreading on rough metal surfaces. *Journal of Materials Science,* **15**, 431-437.

Parent, S.-E., Cabral, A. & Zornberg, J. G. (2007) Water retention curve and hydraulic conductivity function of highly compressible materials. *Canadian Geotechnical Journal,* **44**, 1200-1214.

Pasha, A. Y., Hu, L. & Meegoda, J. N. (2014) Numerical simulations of a light nonaqueous phase liquid (LNAPL) movement in variably saturated soils with capillary hysteresis. *Canadian Geotechnical Journal,* **51**, 1046-1062.

Peters, A. & Durner, W. (2008) A simple model for describing hydraulic conductivity in unsaturated porous media accounting for film and capillary flow. *Water Resources Research,* **44**.

Probst, A., Facius, R., Wirth, R., Wolf, M. & Moissl-Eichinger, C. (2011) Recovery of Bacillus spore contaminants from rough surfaces: a challenge to space mission cleanliness control. *Appl. Environ. Microbiol.,* **77**, 1628-1637.

Quan Lai, C., Thi Mai, T., Zheng, H., Lee, P., Leong, K., Lee, C., *et al.* (2013) Influence of nanoscale geometry on the dynamics of wicking into a rough surface. *Applied Physics Letters,* **102**, 053104.

Rad, M. N. (2014) Pore-Scale Investigation of Salt Precipitation during Evaporation from Porous Media. University of Manchester.

Rawls, W., Gimenez, D. & Grossman, R. (1998) Use of soil texture, bulk density, and slope of the water retention curve to predict saturated hydraulic conductivity. *Transactions of the ASAE,* **41**, 983.

Reddy, A. J., Kokila, M., Nagabhushana, H., Chakradhar, R., Shivakumara, C., Rao, J., *et al.* (2011) Structural, optical and EPR studies on ZnO: Cu nanopowders prepared via low temperature solution combustion synthesis. *Journal of Alloys and Compounds,* **509**, 5349-5355.

Rhoades, K., Eun, J. & Tinjum, J. M. (2015) Transport of hexavalent chromium in the vadose zone by capillary and evaporative transport from chromium ore processing residue. *Canadian Geotechnical Journal,* **53**, 619-633.

Rianna, G., Reder, A. & Pagano, L. (2018) Estimating actual and potential bare soil evaporation from silty pyroclastic soils: Towards improved landslide prediction. *Journal of hydrology,* **562**, 193-209.

Rogers, J. & Klute, A. (1971) The Hydraulic Conductivity-Water Content Relationship During Nonsteady Flow Through a Sand Column 1. *Soil Science Society of America Journal,* **35**, 695-700.

Saiers, J. E. & Lenhart, J. J. (2003) Colloid mobilization and transport within unsaturated porous media under transient-flow conditions. *Water Resources Research,* **39**.

Schindelin, J., Arganda-Carreras, I., Frise, E., Kaynig, V., Longair, M., Pietzsch, T., *et al.* (2012) Fiji: an open-source platform for biological-image analysis. *Nature methods,* **9**, 676.

Shang, J., Flury, M., Chen, G. & Zhuang, J. (2008) Impact of flow rate, water content, and capillary forces on in situ colloid mobilization during infiltration in unsaturated sediments. *Water Resources Research,* **44**.

Singurindy, O. & Berkowitz, B. (2005) The role of fractures on coupled dissolution and precipitation patterns in carbonate rocks. *Advances in Water Resources,* **28**, 507-521.

Tao, F. F. & Salmeron, M. (2011) In situ studies of chemistry and structure of materials in reactive environments. *Science,* **331**, 171-174.

Tokunaga, T. K. (2009) Hydraulic properties of adsorbed water films in unsaturated porous media. *Water resources research,* **45**.

Tokunaga, T. K. (2011) Physicochemical controls on adsorbed water film thickness in unsaturated geological media. *Water Resources Research,* **47**.

Tokunaga, T. K. & Wan, J. (1997) Water film flow along fracture surfaces of porous rock. *Water Resources Research,* **33**, 1287-1295.

Tuller, M. & Or, D. (2005) Water films and scaling of soil characteristic curves at low water contents. *Water Resources Research,* **41**.

Vanapalli, S. & Fredlund, D. (2000) Comparison of different procedures to predict unsaturated soil shear strength. In *Advances in Unsaturated Geotechnics*, pp. 195-209.

Vaunat, J., Romero, E. & Jommi, C. (2000) An elastoplastic hydro-mechanical model for unsaturated soils. *Experimental evidence and theoretical approaches in unsaturated soils,* **20**, 0.

Vorobyev, A. & Guo, C. (2010) Water sprints uphill on glass. *Journal of Applied Physics,* **108**, 123512.

Wang, D., Bradford, S. A., Paradelo, M., Peijnenburg, W. J. & Zhou, D. (2012) Facilitated transport of copper with hydroxyapatite nanoparticles in saturated sand. *Soil Science Society of America Journal,* **76**, 375-388.

Wang, X., Hu, C., Liu, H., Du, G., He, X. & Xi, Y. (2010) Synthesis of CuO nanostructures and their application for nonenzymatic glucose sensing. *Sensors and Actuators B: Chemical,* **144**, 220-225.

Weisbrod, N., Nachshon, U., Dragila, M. & Grader, A. (2014) Micro-CT analysis to explore salt precipitation impact on porous media permeability. In *Transport and Reactivity of Solutions in Confined Hydrosystems*, pp. 231-241. Springer.

Werth, C. J., Zhang, C., Brusseau, M. L., Oostrom, M. & Baumann, T. (2010) A review of non-invasive imaging methods and applications in contaminant hydrogeology research. *Journal of contaminant hydrology,* **113**, 1-24.

Yan, S., Adegbule, A. & Kibbey, T. C. G. (2017) A hybrid 3D SEM reconstruction method optimized for complex geologic material surfaces. *Micron,* **99**, 26-31.

Yang, L., Ge, H., Shi, X., Cheng, Y., Zhang, K., Chen, H., *et al.* (2016) The effect of microstructure and rock mineralogy on water imbibition characteristics in tight reservoirs. *Journal of Natural Gas Science and Engineering,* **34**, 1461-1471.

Yang, Z. P., Zhang, C. J. & Huang, L. N. (2014) Quartz crystal microbalance for comparison of calcium phosphate precipitation on planar and rough phospholipid bilayers. *Colloids and Surfaces B-Biointerfaces,* **116**, 265-269.

Yin, P. & Vanapalli, S. K. (2018) Model for predicting tensile strength of unsaturated cohesionless soils. *Canadian Geotechnical Journal,* **55**, 1313-1333.

Zhang, C., Oostrom, M., Wietsma, T. W., Grate, J. W. & Warner, M. G. (2011) Influence of viscous and capillary forces on immiscible fluid displacement: Pore-scale experimental study in a water-wet micromodel demonstrating viscous and capillary fingering. *Energy & Fuels,* **25**, 3493-3505.

Zhong, K., Yang, X. & Kang, Y. (2010) Effects of ventilation strategies and source locations on indoor particle deposition. *Building and environment,* **45**, 655-662.